Endocytic Uptake of Self-Assembled Iridium(III) Nanoaggregates for Holistic Treatment of Metastatic 3D Triple-Negative Breast Tumor Spheroids

*Ayushi Chaudhary, Ashwini Kumar, Nikhil Swain, Kajal Chaudhary, Himanshu Sonker, Sayari Dewan, Rutwik Anil Patil, and Ritika Gautam Singh**

Triple-negative breast cancer (TNBC) presents a formidable challenge due to its aggressive behavior and limited array of treatment options available. This study focuses on employing nanoaggregate material of organometallic Ir(III) complexes for treating TNBC cell line MDA-MB-231. In this approach, Ir(III) complexes with enhanced cellular permeability are strategically designed and achieved through the incorporation of COOMe groups into their structure. The lead compound, IrL^1, exhibits promiscuous nanoscale aggregation in RPMI cell culture media, characterized by a stable hydrodynamic effective diameter ranging from 190 to 202 nm over 48 h. With excellent photo-responsive contrast-enhanced cell imaging properties IrL^1 exhibits an outstanding IC$_{50,\ 48h}$ value of 36.05± 0.03 nM when irradiated with 390 nm light in MDA-MB-231 (IC$_{50,\ 48\ h}$ of Cisplatin is 5.29 μμ). In cell, investigation confirms that IrL^1 nanoaggregates internalization via energy-dependent endocytosis undergo ferroptosis and ROS mediated cell death in MDA-MB-231 cells. Further, these in vivo studies using NOD-SCID mice confirmed that IrL^1 exhibits a tendency to ablate tumors inoculated in mice models at therapeutically relevant doses. Thus, this comprehensive approach holds promise for expanding the repertoire of organometallic Ir(III) nanoaggregates with adaptable characteristics, thereby advancing their clinical utility of nanomedicine in the holistic treatment of metastatic 3D triple-negative breast tumor spheroids.

1. Introduction

Breast cancer is one of the most widespread malignancies worldwide, explicitly affecting women. Employing gene expression profiling and molecular biology techniques breast cancer can be divided into five distinct clinical subtypes based on histopathological characteristics.[1] Tumor classification based upon PR: progesterone receptor, ER: estrogen receptor, or HER-2: human epidermal growth factor receptor-2 status is indispensable for the evaluation and management of breast cancer treatment.[2] Triple-negative breast cancer (TNBC) represents a subtype characterized by its aggressive clinical behavior compared to other breast cancer subtypes.[3] TNBC comprises tumors with negative expression status for ER, PR, and HER-2 necessitating specialized therapeutic inventions.[4,5] TNBC constitutes ≈10–20% of all breast cancer cases and is frequently detected in patients aged 35 years or younger.[6] It represents a unique form of breast cancer with the poorest prognosis, contributing to 15% of all breast cancer diagnoses and accounting for 25% of related mortalities.[7]

Owing to its notable propensity for metastasis, resistance to traditional chemotherapy and endocrine treatments poses significant clinical challenges. Small molecule targeted therapy involves the development of therapeutic drugs tailored at the molecular level to specifically target defined carcinogenic markers, facilitating tumor cell death upon binding to these targets. Targeted treatment has emerged as a key focus in the treatment of TNBC, leading to the initiation of numerous targeted drug trials. Despite the rapid progress in these developments, the inherent drawback of single-target drug discovery makes TNBC vulnerable to drug resistance. TNBC's tendency for recurrence and distant metastasis contributes to an unfavorable prognosis for patients.[8]

Hence, a rising avenue to tackle this issue includes the development of combination drug strategies, including dual target drugs (designed to address two specific targets simultaneously) and combinations of different drugs. Despite notable progress in apoptosis-based chemotherapy in recent decades,[9,10] the overall efficacy of the current antitumor medications and survival rates of patients with malignant tumors still fall below expectations due to inherent apoptosis resistance observed in various tumor types, notably TNBC. This underscores the urgent need for developing non-apoptotic treatment strategies to effectively eradicate tumor cells.

A. Chaudhary, A. Kumar, N. Swain, K. Chaudhary, H. Sonker, S. Dewan,
R. A. Patil, R. G. Singh
Department of Chemistry
IIT Kanpur
Kanpur, UP 208016, India
E-mail: rgautam@iitk.ac.in

The ORCID identification number(s) for the author(s) of this article can be found under https://doi.org/10.1002/smll.202406809

DOI: 10.1002/smll.202406809

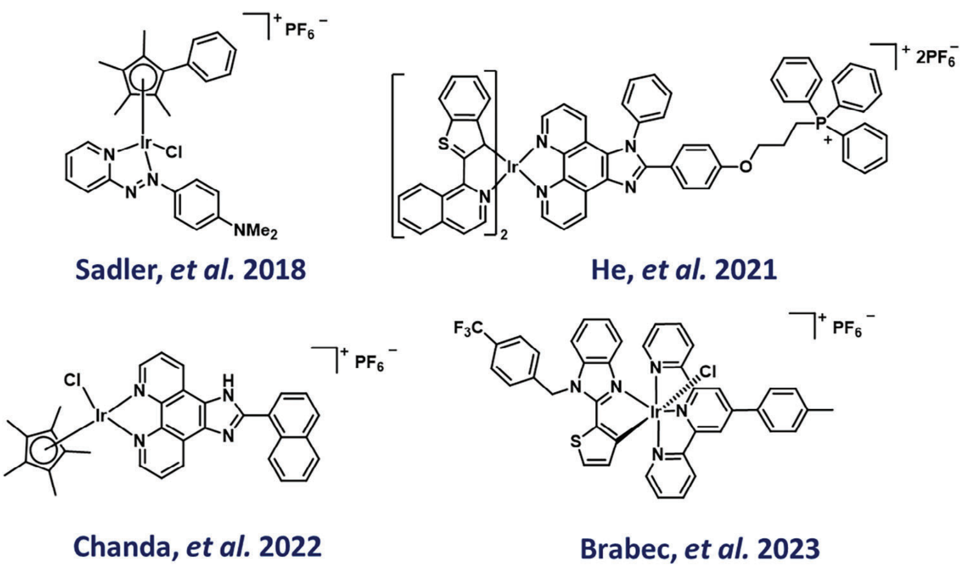

Figure 1. Previously reported Ir(III)-based medications with a potential to treat Triple-Negative Breast Cancer (TNBC).

Ferroptosis, a recently recognized mode of regulated cell death (RCD) is characterized by the abnormal accumulation of cytotoxic-iron mediated lipid peroxides. Unlike extensively studied RCD forms like necrosis and apoptosis, ferroptosis has garnered significant attention for its potential in treating apoptosis-resistant tumors.[11]

Recently, metal-based medications have demonstrated potential in treating TNBC, including several organometallic compounds. Clinical trials predominantly explore the combinations of conventional chemotherapy agents like cisplatin, carboplatin, oxaliplatin, gemcitabine, paclitaxel, or lxabepilone along with inhibitors targeting growth factor receptors such as Erlotinib, kinase inhibitors (like Everolimus), check-point inhibitors (such as Imprime), or antibodies (such as Bevacizumab, Cetuximab).[12]

Organometallic Ir(III) complexes have been extensively studied, for their potential as anticancer agents, utility in contrast-enhanced cell imaging, and labeling of peptides.[13–17] However, the effectiveness and mechanisms of iridium compounds in treating TNBC remain unclear. A preliminary study utilizing organo-iridium (III) complexes synthesized by Sadler et. al exhibited enhanced anti-proliferative properties in TNBC cell lines MDA-MB-468 and OCUB-M during screening with the National Cancer Institute (NCI) 60 cell line, particularly the iridium-phenylazopyidine complex.[18] In 2021 He et al. illustrated the combined impact of ferroptosis and apoptosis in hindering the growth of triple-negative MDA-MB-231 cells by utilizing mitochondria-targeting Ir(III) cyclometalated compounds.[19] In 2022, Chanda and coworkers synthesized half-sandwich cyclometalated Ir(III) complexes, inducing mitochondrion-mediated apoptosis in the TNBC cell line MDA-MB-468.[20] A recent study by Brabec et al. in 2023 underscored the effectiveness of octahedral Ir(III) complexes in effectively inhibiting metastatic processes in the triple-negative breast cancer cell line MDA-MB-231 (**Figure 1**).[21a]

However, despite its several benefits, Iridium(III) based complexes face significant challenges such as poor uptake, lack of specificity, extensive biological distribution, brief half-life, and systemic toxicity. A variety of prodrug systems have been developed to address this challenge, including nanoparticles, liposomes, and polymers. Among these, polymeric systems are often favored due to their ability to incorporate numerous functional groups. This versatility enables them to mitigate issues related to poor pharmacokinetics, inappropriate distribution, and low solubility, thereby enhancing drug clearance rates. To overcome these challenges, we designed, synthesized, and characterized a series of novel organometallic Ir(III) complexes-based nanoaggregates with the inclusion of methyl ester (-COOMe) groups aims to enhance the lipophilicity and cell permeability of the complexes. Many FDA-approved drugs, such as oseltamivir, aspirin, and enalapril, utilize esterification to improve bioavailability and absorption. Moreover, fluorescent dyes such as calcein-AM, fluorescein diacetate, and Fluo-3 AM are commonly used in esterase-mediated delivery inside cells. Based on these well-established precedents, we designed our Iridium(III) complexes incorporating methyl ester groups, with the expectation that they would contribute to enhanced cellular uptake and lipophilicity.[21b–d] Notably, these Ir(III) complexes exist as in situ generated nanoscale aggregates in biological cell culture media. These nanoaggregates tend to co-localize in the endoplasmic reticulum and mitochondria and exhibit unique photophysical, biological, and pharmacological behavior that can be utilized for therapeutic advantage. Our study indicates that the core of Ir(III) nanoaggregates is a highly conjugated system that absorbs light, enabling efficient energy transfer to generate ROS. These ROS with tumor or subcellular organelle targeting properties can alter cellular uptake, organ accumulation, and many aspects of pharmacokinetics and pharmacodynamics (PK/PD). The prodrug Ir(III) nanoaggregates generated ROS depletes intracellular GSH and inhibits glutathione peroxidase 4, a GSH-dependent hydroperoxidase, to cause lipid peroxidation and eventually act as a ferroptosis-based cell death inducer in TNBC cell line MDA-MB-231. Additionally, the remarkable imaging potential of these Ir(III) nanoaggregates assists in monitoring the dynamic behavior of subcellular organelles and the changes in the microenvironment. The

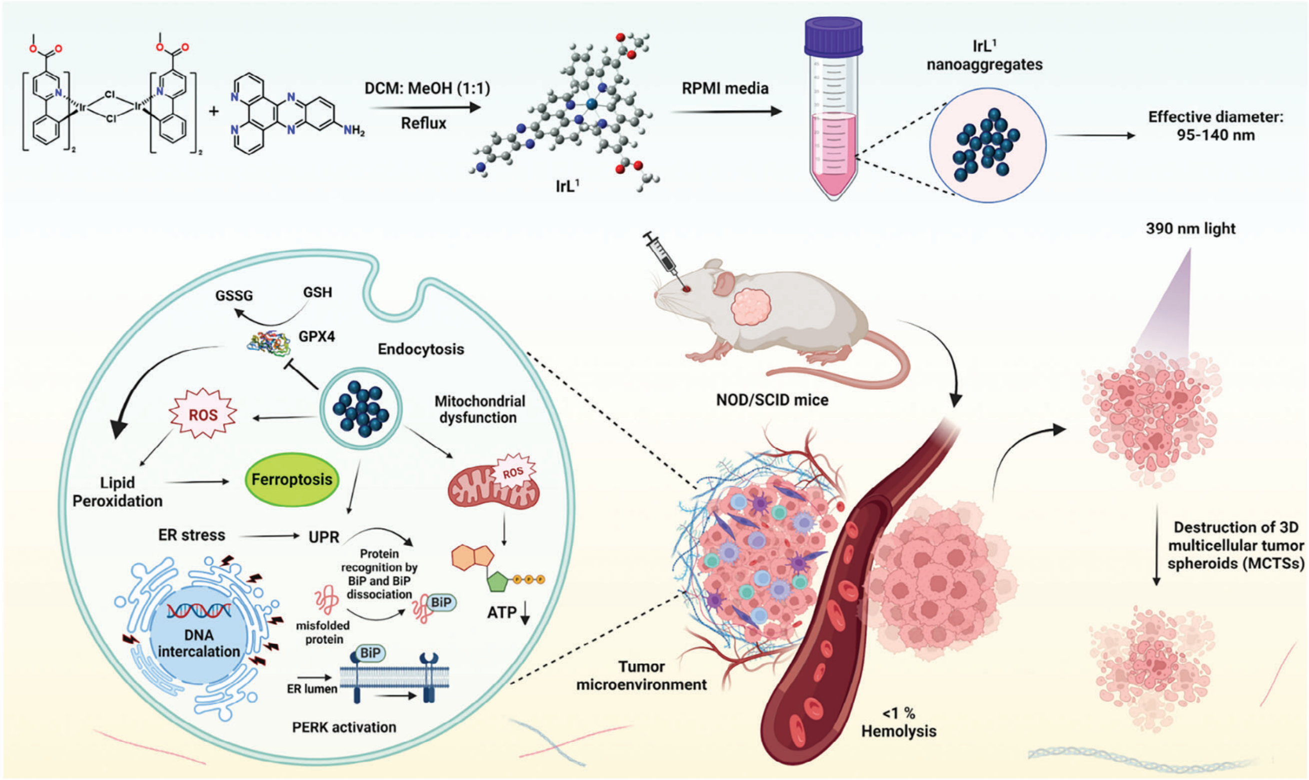

Figure 2. Schematic illustration of IrL^1 nanoaggregates unveiling ferroptosis mediated cell death in 4T1 tumor-bearing mice.

anticancer response of IrL^1 has been well studied including the mechanism of cellular uptake, its effect on other cellular organelles, and in vivo investigations (**Figure 2**) circumventing the limitations associated with using doxorubicin in conventional TNBC chemotherapy. Finally, our comprehensive research initiative has capabilities to transcend the confines of our laboratory, heralding a pivotal step toward the ability to combine both therapeutic and diagnostic capabilities into a single nanoaggregate-based complex and advancing the frontiers of nanomedicine with a profound clinical implication.

2. Result and Discussion

2.1. Design and Synthesis of Ir(III) Complexes

Our approach focused on the meticulous design and synthesis of Iridium(III) cyclometalated complexes, motivated by their outstanding anticancer activity. Additionally, we aimed to leverage their potential for precise organelle targeting and advanced intracellular imaging capabilities.[22,23] To accomplish this objective, we systematically synthesized a series of novel Ir(III) complexes using L^1–L8 ligands as shown in **Figure 3**. The significance of these synthesized complexes lies in their meticulously chosen molecular moieties, as illustrated in Figure 3. The ligands were synthesized from Suzuki coupling using 2-bromo-isonicotinic acid and boronic acids with substituted groups at X and Y. Within the ligand scaffold, various biologically relevant groups were strategically incorporated. Notably, the inclusion of methyl ester (-COOMe) groups aims to enhance the lipophilicity and cell permeability of the complexes.[24] Additionally, these COOMe groups serve as functionalization handles, facilitating the attachment of targeting ligands that can specifically bind to receptors overexpressed on cancer cell surfaces, thereby minimizing off-target effects, and enhancing therapeutic efficacy. MDA-MB-231 cells lack major receptors that would directly interact with ester groups. However, these cells do express carboxylesterase enzymes capable of hydrolyzing ester bonds, which could convert prodrugs into their active or inactive forms. Moreover, the integration of the phenanthroline moiety provides a versatile platform, endowing the complexes with a high affinity for DNA binding through intercalation or groove binding.[25] Detailed synthesis procedures and characterization data for both ligands and complexes are provided in the supporting Information (Figures S1–S24, Supporting Information). All complexes (Figure 3) were thoroughly characterized by various spectroscopic techniques, ^1H and $^{13}C\{^1H\}$ NMR, FT-IR, UV–vis, and ESI-MS, and their purity was assessed by RP-HPLC and determined to be > 95%. The FT-IR spectra of the metal complexes are shown in Figure S25, Supporting Information. The FT-IR spectra of Ir(III) complexes displayed bands at 550–560 cm^{-1} ν(P—F) 1400–1590 cm^{-1} $\nu(C{=}C_{aromatic})$, 2905–2925 cm^{-1} $\nu(C{=}N_{py})$, 1715–1735 cm^{-1} ν(C=O), 3380–3395 cm^{-1} ν(N—H). Notably, the complexes exhibited solubility in common organic solvents including DMSO, DMF, MeOH, CH_3CN, CH_2Cl_2, and THF. Crystallographic data for ligand L^3 and intermediate dimer complex $Ir_2Cl_2(L^3)_4$ are summarized in Tables S3 and S5 (Supporting Information) the selected bond angles and bond lengths are provided in Tables S4 and S6 (Supporting Information). The

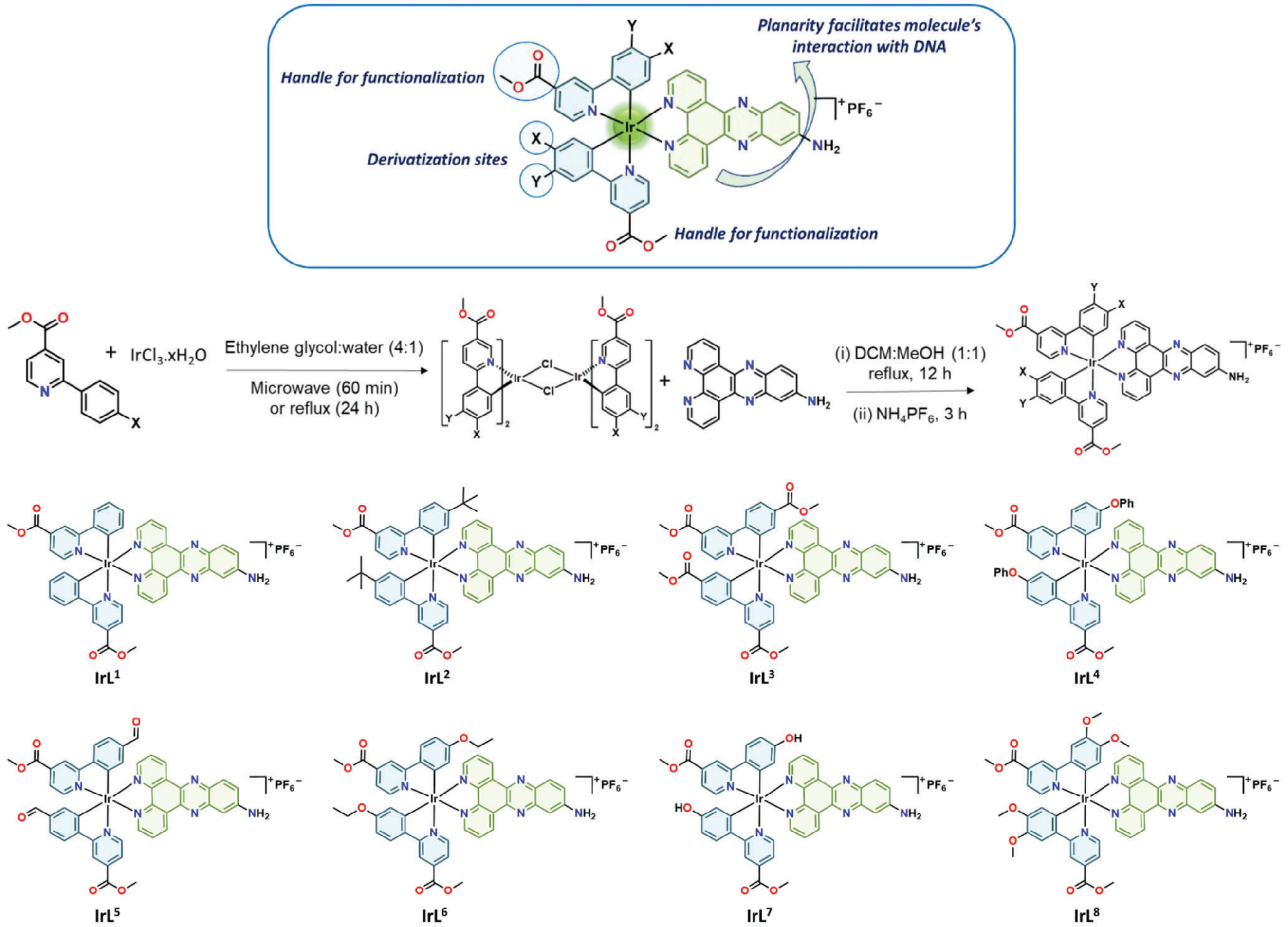

Figure 3. Design and synthesis scheme of Ir(III) complexes.

DFT calculations have also been performed on all the complexes and the molecular orbital (MO) distribution is represented in **Figure 4**.

2.2. Photophysical Properties in Solution

The absorption spectra of ligands and their corresponding complexes in DMSO at 298 K are reported in Figures S26 and S27 (Supporting Information). The 290–350 nm spectral window displays the intense absorption bands ($\epsilon \approx (0.5–2) \times 10^5$ M^{-1} cm^{-1}) that represent spin-allowed ligand-centered (LC) $\pi–\pi^*$ transitions which involve both the (N^N) type ancillary ligands and the (C^N) cyclometalated ligands.[26,27] On the other hand, the bands at longer wavelengths (450–480 nm; $\epsilon \approx (1–5) \times 10^4$ M^{-1} cm^{-1}) correspond to the metal-to-ligand charge transfer transitions (MLCT).[28] The emission spectra of the Ir(III) complexes 298 K in DMSO are shown in Figure S28 (Supporting Information), and the emission spectra of ligands in DMSO and 1X PBS are depicted in Figure S26 in Supporting Information. The luminescence properties and photophysical parameters of Ir(III) complexes and ligands are summarized in **Table 1**. All the Ir(III) complexes displayed green emission with maxima between 550–590 nm. The emission property indicates that Ir(III) complexes can be utilized for intracellular imaging and as a diagnostic sensor.

2.3. Stability and Lipophilicity Profile

The stability of Ir(III) complexes was assessed using UV–vis absorption spectroscopy in a tris-buffer solution at pH 7.4. As depicted in Figure S29 (Supporting Information), the UV–vis spectra of IrL^1–IrL^8 showed a consistent pattern without any discernible hypsochromic or bathochromic shifts observed at 0, 24, and 48 h, suggesting that IrL^1–IrL^8 maintained stability in solution at room temperature over 48 h. Given that along with stability, the cellular uptake of the drugs is significantly influenced by factors such as water solubility, alongside mechanisms of cellular uptake and molecular size,[29] we initially examined the lipophilicity index of Ir(III) complexes before embarking on anticancer studies. The lipophilicity of these compounds was quantified by their log $P_{o/w}$ values (partition coefficient in n-octanol/water system), as detailed in Table S2 (Supporting Information). The log $P_{o/w}$ values suggest that the Ir(III) complexes are moderately lipophilic in nature.

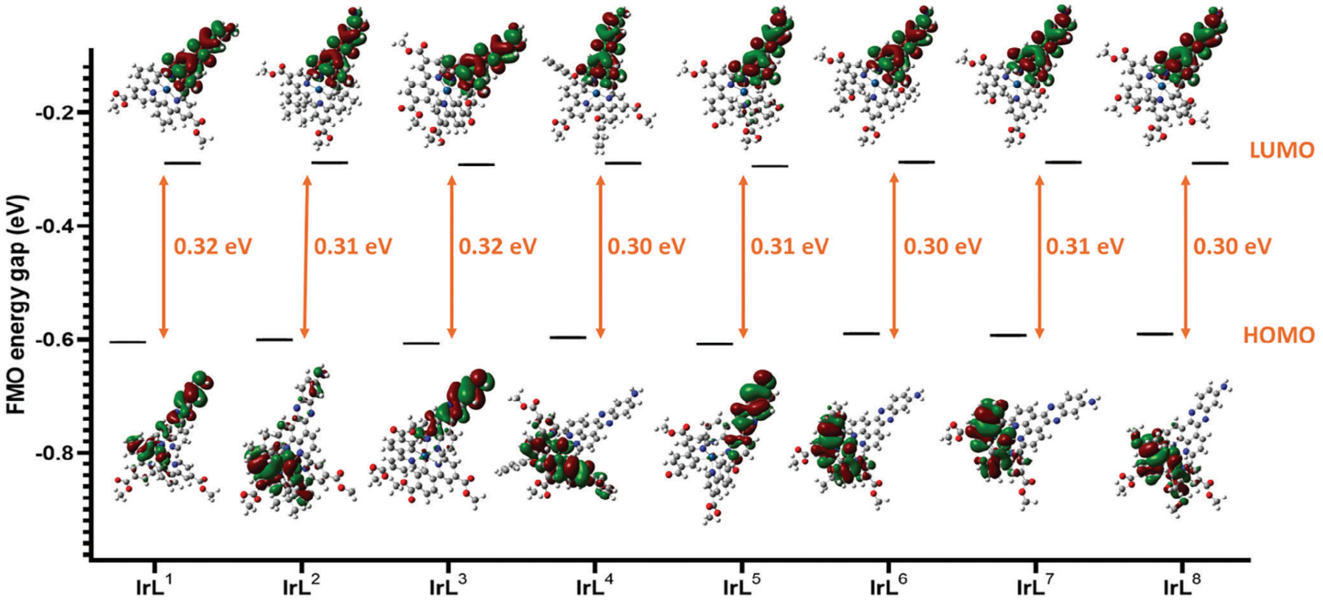

Figure 4. Illustrations of Frontier molecular orbitals, HOMOs, and LUMOs of Ir(III) complexes determined by DFT at B3LYP functional along with 6–31G** and LANL2DZ for Ir(III).

2.4. IrL^1 Nanoaggregates Formation and Characterization

After the characterization of the monomeric IrL^1 complexes, the corresponding nanoaggregates condition and formation were explored. To comprehend the behavior of the nanoaggregate formation in the cell culture media, we delved into the phenomenon of self-assembly and conducted Dynamic Light Scattering (DLS) measurements on a solution of IrL^1 in RPMI media at a final concentration of 3 μμ. Remarkably, our findings unveiled the immediate formation of self-assembly of IrL^1, characterized by a hydrodynamic effective diameter ranging from 190 to 202 nm. Importantly, this self-assembled state remained unchanged over a period of 48 h (**Figure** 5). For a comprehensive understanding of the aggregation, the solution of IrL^1 in RPMI media was examined using scanning electron microscopy (SEM) and high-resolution transmission electron microscopy (HRTEM) techniques. In solution, IrL^1 exhibited aggregated particles with an average size of ≈95–140 nm (Figure 5b). The observed morphology of IrL^1 nanoaggregates that appeared in the HRTEM resembles the nanodots.[30] The selected particles have a spacing of 0.28 nm (Figure 5c.) Energy-dispersive X-ray (EDX)-TEM and EDX-SEM analysis further confirmed the presence of IrL^1 within these particles (Figures S39 and S40, Supporting Information).

2.5. Anticancer Profile of Ir(III) Complexes

Following detailed solid state and solution characterization of Ir(III)-nanoaggregates, the complexes IrL^1–IrL^8 were screened against a series of cancer cell lines namely, breast adenocarcinoma cell lines MDA-MB-231 and MCF-7, Human lung adenocarcinoma cell line A549, human prostate cancer cell line PC3, Human colon cancer cell line HCT-116, and normal human embryonic kidney cell line HEK-293, using FDA approved cisplatin as the positive control. **Table** 2 demonstrates the $IC_{50,48h}$ value of the Ir(III) complexes determined by the MTT assay. In the antiproliferative assay IrL^1 displayed highest cytotoxicity with IC_{50} value on MDA-MB-231 (0.33 μμ), A549 (0.82 μμ), MCF-7 (0.64

Table 1. Absorption and emission spectra of ligands and their corresponding Ir(III) complexes were recorded in DMSO at room temperature. The emission spectra of Ir(III) complexes were recorded upon excitation (400–460 nm) in the MLCT region. Quantum yields (Φ) were measured in DMSO at room temperature using fluorescein (Φ = 0.79, 0.1 м NaOH) as the reference.

Compound	$\lambda_{\text{abs, nm}}$ [ϵ/ 10^3 M^{-1} cm^{-1}]	$\lambda_{\text{em, nm}}$	Compound	$\lambda_{\text{abs, nm}}$ [ϵ/ M^{-1} cm^{-1}]	$\lambda_{\text{em, nm}}$	Φ
L1	302 (5.50)	356	IrL^1	327 (1.70×10^5), 476 (5.0×10^4)	586	0.01
L^2	303 (5.01)	387	IrL^2	331 (1.45×10^5), 475 (3.19×10^4)	581	0.01
L^3	296 (7.32)	362	IrL^3	295 (1.53×10^5), 469 (2.64×10^4)	561	0.04
L4	237 (6.42)	418	IrL^4	325 (1.91×10^5), 477 (4.11×10^4)	589	0.02
L5	303 (6.61)	392	IrL^5	328 (5.84×10^4), 473 (1.32×10^4)	584	0.01
L6	291 (7.78)	435	IrL^6	329 (1.25×10^5), 475 (3.23×10^4)	581	0.09
L7	291 (7.73)	393	IrL^7	327 (1.33×10^5), 473 (3.45×10^4)	587	0.01
L8	320 (5.31)	479	IrL^8	327 (1.11×10^5), 477 (3.51×10^4)	558	0.0007

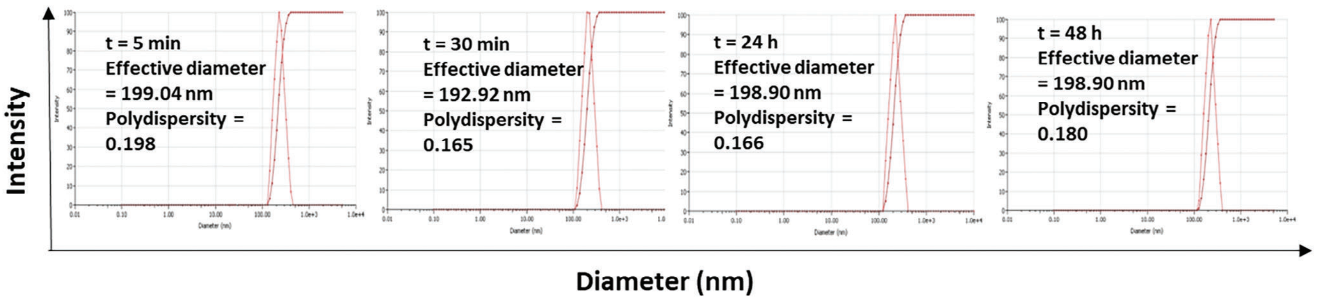

Figure 5. DLS data at different time intervals of a solution of IrL^1 in RPMI cell culture media. (SEM images of IrL^1 nanoaggregates and HRTEM images of IrL^1 nanoaggregates are shown in Supporting Information).

Table 2. Half-maximum (50%) Inhibitory concentrations (IC_{50}, μμ) of IrL^1–IrL^8 determined by the MTT assay after exposure of Ir (III) complexes for 48 h.

Cell growth inhibition, IC_{50} (μμ), 48 h

Compounds	MDA-MB-231	MCF-7	A549	PC3	HCT-116	HEK-293
IrL^1	0.33 ± 0.05	0.64 ± 0.04	0.82 ± 0.19	0.51 ± 0.30	1.27 ± 0.15	2.45 ± 0.87
IrL^2	2.50 ± 1.70	1.13 ± 0.33	4.81 ± 1.66	4.85 ± 1.42	1.60 ± 0.07	0.96 ± 0.42
IrL^3	>25	>25	>25	>25	>25	>25
IrL^4	1.48 ± 1.14	1.78 ± 0.16	0.96 ± 1.48	6.02 ± 3.84	6.19 ± 1.98	1.83 ± 1.46
IrL^5	>25	>25	>25	>25	>25	>25
IrL^6	1.0 ± 0.47	0.47 ± 0.07	1.74 ± 0.45	0.97 ± 5.08	2.00 ± 0.43	2.06 ± 2.18
IrL7	>25	>25	>25	>25	>25	>25
IrL^8	>25	>25	>25	>25	4.09 ± 2.17	>25
Cisplatin	5.29 ± 0.25	7.0 ± 4.51	11.12 ± 2.55	3.13 ± 0.22	5.38 ± 2.57	2.66 ± 0.71

μμ), HCT-116 (1.27 μμ) and PC3 (0.51 μμ) compared to rest of the Ir(III) complexes, indicating that IrL^1 is more cytotoxic than cisplatin. IrL^1 displayed significant cytotoxicity on the MDA-MB-231 cell line, compared to other screened cancer cells, indicating its specificity in cytotoxicity on the triple-negative breast cancer cell line. The photocytotoxicity of IrL^1 was also investigated on MDA-MB-231 cells. Upon exposure to 390 nm light (0.363 mW cm^{-2} 25 min), IrL^1 demonstrated exceptional photocytotoxicity with an $IC_{50,48\ h}$ value of 36.05 ± 0.03 nμ on MDA-MB-231 cells. (**Figure 6**). We conducted the cytotoxicity experiment under the same conditions of light irradiation on healthy kidney cell line HEK-293. The results obtained indicated no pronounced effect of light irradiation on the HEK-293 cell line. However, the cytotoxicity of the compound increased ≈10 times on MDA-MB-231 cells. These results display the selectivity of the complex toward cancer cells upon light irradiation. (Figure S52 and Table S8, Supporting Information). Conversely IrL^1 showed comparable antiproliferative activity with cisplatin on HEK-293 (IrL^1, $IC_{50,\ 48\ h}$ = 2.45 μμ; Cisplatin, $IC_{50,\ 48\ h}$ = 2.66 μμ). Hence, IrL^1 was solicited for further mechanistic studies (Figure S41, Supporting Information).

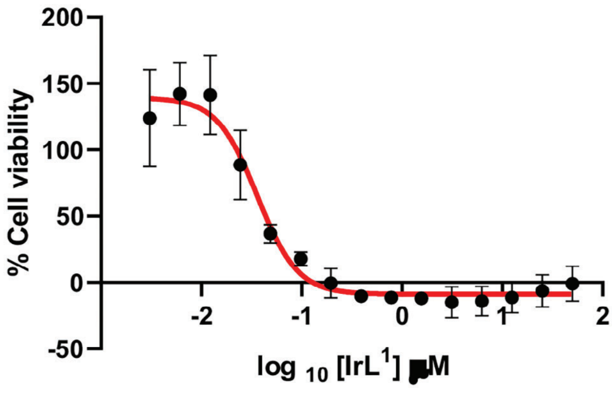

Figure 6. Percentage cell viability of MDA-MB-231 cells treated with IrL^1 under light exposure (390 nm, 0.363 mW cm^{-2}, 25 min).

The efficacy of the drugs is affected by their ability to be taken up by cellular structures. We discovered that IrL^1 had a more pronounced cytotoxic effect on MDA-MB-231 cells compared to other cell types. Consequently, for our further investigations, we focused on the intracellular uptake of IrL^1 and $IrCl_3.xH_2O$ in MDA-MB-231 cells using inductively coupled plasma mass spectrometry (ICP-MS). After an 8 h treatment with IrL^1, we observed a significant increase in intracellular Iridium content in MDA-MB-231 cells compared to the control group and cells treated with $IrCl_3.xH_2O$ (**Figure 7b**). The order of cellular uptake was IrL^1 > $IrCl_3.xH_2O$ > control. These results clearly indicate that the cellular uptake of IrL^1 is notably higher than that of the corresponding metal salt $IrCl_3.xH_2O$. Furthermore, our findings suggest a correlation between the antiproliferative activity of IrL^1 and its cellular uptake efficiency, as seen in both cytotoxicity assays and cellular uptake measurements.

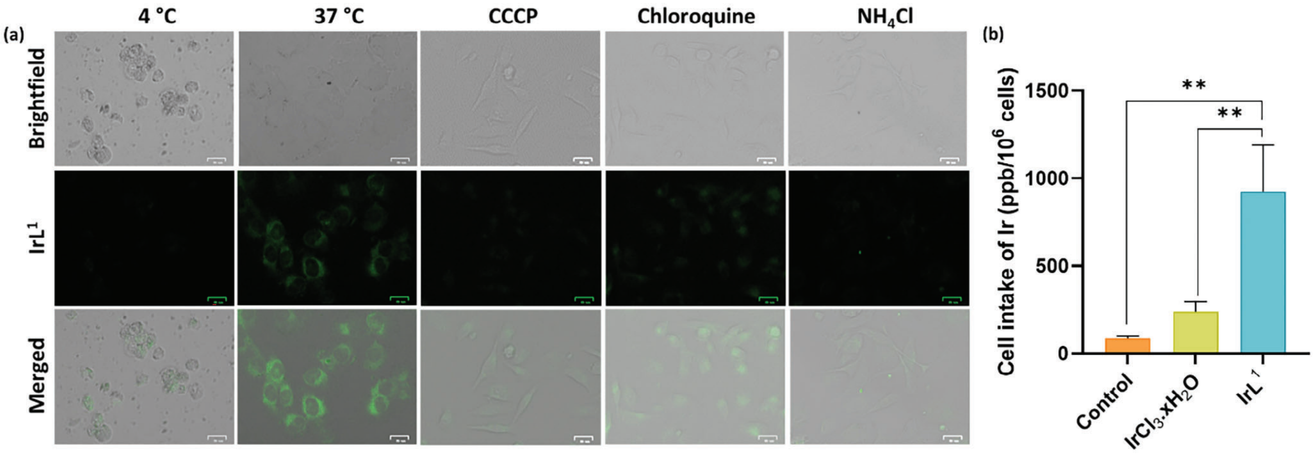

Figure 7. The Cellular uptake mechanism of IrL^1. a) MDA-MB-231 cells were stained with Ir(III) complex (1.65 μм, 2 h) under different conditions by varying the temperature (4 °C and 37 °C) as well as the addition of metabolic inhibitor (CCCP) and endocytic inhibitors (chloroquine and NH$_4$Cl). Scale bar: 25 μm. b) ICP-MS assay of total cell uptake after treatment with 6.6 μм IrL^1 and IrCl$_3$.xH$_2$O in MDA-MB-231 cell line for 8 h at 37 °C. The untreated cells were taken as the control. Each data point represents mean ± SD, $n = 3$. **$p < 0.01$.

2.6. Mechanism of Cellular Uptake

To identify the specific uptake mechanism and to explore the pathway by which the drug reaches its intended target within the cell we extended our study to investigate the mechanism of cellular uptake. Drugs can be taken up by different pathways like passive diffusion, active transport, endocytosis, facilitated diffusion, and macropinocytosis but for nanoaggregates, they generally enter cells by endocytosis via energy-dependent or energy-independent pathways.[31a] Although we have incorporated different functional groups, the lipophilicity results indicate moderate lipophilicity of all the complexes. Thus, we ruled out their possibility to enter the cells by passive diffusion. Therefore, we moved on to investigate the cellular uptake mechanism via active transport; energy-dependent uptake, and endocytosis. For this purpose, we incubated MDA-MB-231 cells with IrL^1 at 4 °C and treated them with the metabolic inhibitor (CCCP). It results in a decreased fluorescence of IrL^1 compared with the IrL^1 treated cells at 37 °C, this indicates the energy-dependent mechanism. The decreased fluorescence was also observed when cells were pretreated with the endocytosis inhibitor NH$_4$Cl and chloroquine (Figure 7a). NH$_4$Cl and chloroquine are weak bases that can accumulate within the acidic vesicles and result in raising the pH of these vesicles. By increasing the pH both substances can interfere with the normal acid-dependent processes that are crucial for endocytosis. As a result, the endocytosis was inhibited, and the results obtained indicated that IrL^1 enters MDA-MB-231 cells by the energy-dependent endocytosis pathway.

2.7. Self-Assembly Behavior

To better understand the self-assembly, nanoaggregates formation, and the role of media proteins in the stabilization of these nanoaggregates, we performed DLS, HR-TEM, and DLS of all the IrL^1–IrL^8 complexes in RPMI media without FBS protein. As shown by the DLS and TEM data provided in Figures S46–S48 (Supporting Information), the complexes IrL^1, IrL^2, IrL^4, and IrL^6 were found to possess aggregation in the range 200–400 nm, whereas the remaining metal complexes possessed hydrodynamic diameter >1000 nm in the culture media. Also, in the previous cytotoxicity experiment conducted, we found that these complexes which are found to form nanoaggregates displayed significant cytotoxicity compared to the remaining ones. Thus, to investigate this reason so as to why these complexes displayed such behavior, the DLS investigation of the active compounds in the culture medium in the absence of FBS was performed (Figure S49, Supporting Information), as it is documented in the literature that the serum proteins in the culture medium can stabilize the nanoaggregates formation.[31b] The results obtained indicated that in the absence of FBS, particles with hydrodynamic diameter >1000 nm were formed, resulting in the precipitation of these complexes, indicating the role of serum proteins in the formation and stabilization of the nanoaggregates. Thus, these nanoaggregates were formed through π–π stacking and were stabilized in a culture medium with the help of serum proteins, in the absence of which these complexes precipitated.

2.8. Rationale for Nanoaggregate Formation

The formation of nanoaggregates is a complex process governed by a range of non-covalent interactions, including hydrogen bonding, hydrophobic forces, electrostatic interactions, π–π stacking, and van der Waals forces.[31c,d] These forces collectively drive the self-assembly of small molecules, with each type of interaction playing a dominant role depending on the molecular system under study. In the context of our research, the observed differences in nanoaggregation behavior among the complexes IrL^1, IrL^2, IrL^4, IrL^6, and others can be primarily attributed to variations in their hydrophobicity and π–π interactions. Lipophilicity data (Table S2, Supporting Information) indicate that IrL^1, IrL^2, and IrL^6, containing unsubstituted, tert-butyl, and ethoxy functional groups respectively, exhibit greater hydrophobicity compared to the other complexes. In aqueous environments such as cell culture media, these hydrophobic interactions drive the aggregation process, as the molecules tend to cluster to minimize their exposure to the surrounding aqueous phase.[31e,f] On the other hand, complexes such as IrL^5, IrL^7, and IrL^8 are relatively more hydrophilic, likely due to the presence of polar functional groups, including formyl, hydroxyl, and methoxy moieties. Complexes IrL^3, IrL^5, IrL^7, and IrL^8 displayed particle sizes exceeding 1000 nm in the culture medium, possibly due to stronger intermolecular hydrogen bonding, which resulted in poor solvation and, consequently, larger aggregate formation. Hydrogen bonding is known to have a dual role, potentially reducing or enhancing drug dissolution rates depending on the system.[31g] The tendency of IrL^1, IrL^2, IrL^4, and IrL^6 to form nanoaggregates can be explained by their higher lipophilicity and stronger π–π stacking interactions compared to the other complexes, thus rationalizing their self-assembly behavior in our experimental conditions.

2.9. Intracellular Localization of IrL^1

Phosphorescent iridium(III) complexes possess unique excited-state properties including high luminescence quantum yields, tunable phosphorescence wavelengths, large Stokes shifts, long phosphorescence lifetimes, and high chemical and photochemical stability. This renders them suitable for a broad spectrum of applications, encompassing cellular imaging reagents, labeling reagents, biosensors, cytotoxic drugs, and photosensitizers. To visualize the intracellular localization of IrL^1 we utilize its emissive property. Here, MDA-MB-231 cells were incubated with IrL^1, and organelle-specific staining dyes were utilized to examine intracellular localization (MitoTracker Deep Red, LysoTracker Deep Red, and ER-Tracker Red). The co-stain pattern of IrL^1 matched with those of MitoTracker Deep Red, and ER-Tracker Red with the considerable value of Pearson correlation coefficient (≈90%) in the scatter plot, which suggests preferential accumulation of IrL^1 in the mitochondria and endoplasmic reticulum (**Figure** 8a).

2.10. Investigation of Ferroptosis Mediated Cell Death Pathway

To investigate the mode of cell death pathway, the cytotoxicity of IrL^1 was determined in presence of various inhibitors mainly Z-VAD–fmk (apoptosis inhibitor), cycloheximide (paraptosis inhibitor), Necrostatin-1 (necroptosis inhibitor), NAC (ROS scavenger), 3-methyl adenine (autophagy inhibitor), and ferrostatin-1 (ferroptosis inhibitor). The IC$_{50,\ 24\ h}$ value of IrL^1 increased from 2.33 to 11.08 μμ and 14.33 μμ in the presence of ferrostatin-1 and N-acetyl cysteine (NAC) respectively (Figure 8b), suggesting the ferroptosis-mediated cell death mechanism.

2.11. Ferroptosis Triggered by IrL^1

Investigation of the mode of cell death by incubating IrL^1 with different inhibitors suggests that none of the inhibitors displayed a clear influence on reduction in cell viability except for ferrostatin-1 treated cells, indicating that IrL^1 causes ferroptosis. Based on these results, we thoroughly verified the common ferroptosis markers, namely reactive oxygen species (ROS) generation, Glutathione depletion, lipid peroxidation, and inhibition of glutathione-dependent antioxidant enzyme glutathione peroxidase 4 (GPX4).[32,33] We initiated our study by investigating the electrochemical redox profile of IrL^1 by cyclic voltammetry (CV) in anhydrous acetonitrile. The compound IrL^1 exhibited an irreversible behavior during the anodic scans whereas it exhibited reversible behavior during the cathodic scans. The irreversible oxidation peak at +1.28 V was attributed to Ir^{IV}/ Ir^{III} as shown in Figure S42 (Supporting Information).[34] The redox nature of IrL^1 was further confirmed by ROS assay. As shown in the Figure 8c. IrL^1 causes extensive ROS generation as observed by cell permeating dihydrodichlorofluorescein diacetate (DCFH-DA) that gets hydrolyzed intracellularly to produce a dihydrodichlorofluorescein (DCFH) probe, which is oxidized to produce the bright green, fluorescent product dichlorofluorescein (DCF). The increase in the DCF emission intensity was detected by the fluorescent cell imager after 3 h of IrL^1-treatment, suggesting ROS elevation with the increase in the concentration of IrL^1 in the cells. However, no distinct increase in fluorescence intensity of DCF was detected by adding the ROS scavenger N-acetyl cysteine (NAC) in advance, suggesting that IrL^1 was indeed capable of generating ROS in the cells (Figure 8c; Figure S43, Supporting Information). The BODIPY 581/591 C11 probe was used to detect and quantify lipid peroxidation (LPO) using fluorescent microscopy and flow cytometry. Oxidation of the polyunsaturated butadienyl portion of the dye results in a shift of the fluorescence emission peak from ≈590 nm (red) to ≈510 nm (green).[35] Notably, IrL^1 caused increased lipid peroxidation as shown in Figure 8d,e. The antioxidant glutathione (GSH) is used as a defense tool by cancer cells as it can consume ROS to hinder cell death.

To measure the change in the GSH level in MDA-MB-231 after treatment with IrL^1, a GSH-Glo assay was performed. This is the luminescence-based assay which is utilized for quantification and detection of GSH levels in cells. This assay relies on the conversion of luciferin derivative into luciferin in the presence of glutathione and this reaction is catalyzed by the glutathione S-transferase enzyme provided in the kit. The luciferin formed is detected by its reaction with Ultra-Glo Recombinant luciferase (provided in the GSH-Glo Glutathione assay kit, Promega) that generates luminescence which is proportional to the amount of GSH present in the cell. As shown in Figure 8f, the GSH concentration was decreased significantly in treated cells when compared to the control. Further to analyze the cause of ROS generation we detected the change in the expression of GPX4 by western blot. GPX4, the glutathione-dependent enzyme, reduces lipid hydroperoxides to lipid alcohol and limits the iron-dependent formation of lipid alkoxy radicals from lipid hydroperoxides.[36] The western blot result clearly shows the inhibition of GPX4 with the increasing concentration of IrL^{1,} at the highest drug dose the GPX4 intensity was ≈90% less than that of the control, which led to the accumulation of lipid ROS, and eventually cell death (Figure 6g).

2.12. IrL^1 Interplay With Cellular Organelles (Endoplasmic Reticulum Stress and Mitochondrial Dysfunction)

The primary interaction between therapeutic agents and cells is dependent on the subcellular target. The endoplasmic

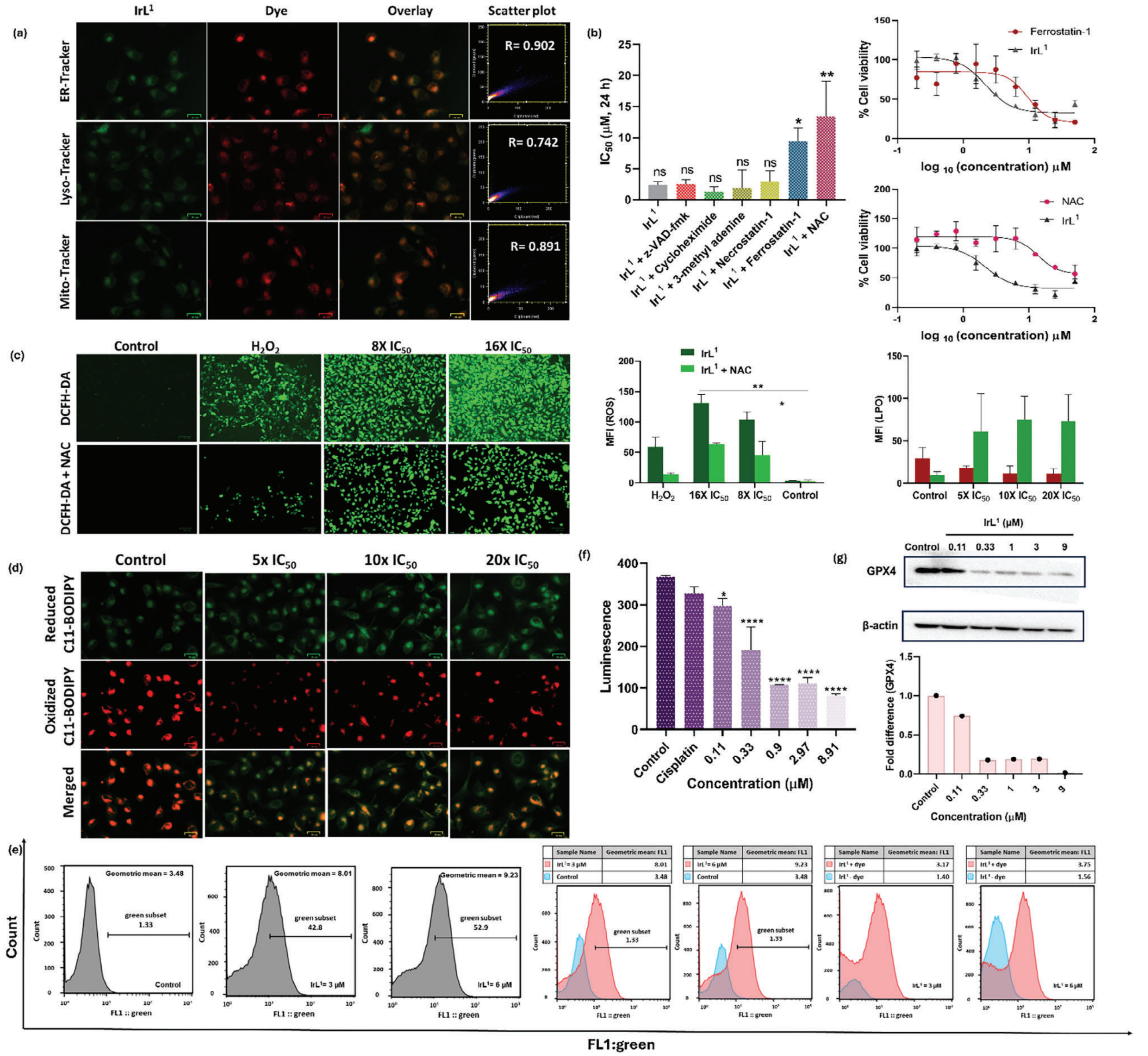

Figure 8. a) Co-localization of IrL¹ by BIO-RAD ZOE fluorescent cell imager. MDA-MB-231 cells were incubated with IrL¹ (3.3 μм, 3 h) and then respectively incubated with ER-Tracker Red, MitoTracker Deep Red FM, or LysoTracker Deep Red DND-26 for 0.5 h after being washed with PBS. Scale bar 25 μm. Ferroptosis triggered by IrL¹. b) Cell viabilities of MDA-MB-231 with the coincubation of various inhibitors and IrL¹ complex. Each data point represents mean ± SD, n =3. Significantly compared to IrL¹: $^{**}p < 0.01$, $^{*}p < 0.1$ ns= non-significant. c) Measurement of intracellular ROS levels by DCFH-DA assay. H_2O_2 and untreated cells were taken as positive and negative controls respectively. Scale bar: 100 μm. d) Fluorescent images of C11-BODIPY dye–stained MDA-MB-231 cells after being incubated with IrL¹ IC_{50} for 0.5 h. Untreated cells were taken as the negative control. Scale bar: 25 μm. The fluorescence was monitored by a BIO-RAD ZOE fluorescent cell imager. The mean fluorescence intensity was calculated using Image J software. e) Lipid peroxidation in MDA-MB-231 cells treated with 3 and 6 μм IrL¹ with untreated cells as the control, determined by BODIPY-C11 staining via flow cytometry after 3 h incubation () Decrease of cellular GSH levels in MDA-MB-231 cells incubated with IrL¹. The luminescence intensity was measured using a microplate reader. Each data point represents mean ± SD, n =3. Significantly compared to control: $^{****}p < 0.0001$, $^{*}p < 0.1$. g) Analysis of expression of GPX4 by western blot. The fold change in expression of GPX4 in MDA-MB-231 cells treated with IrL¹ (0.11–9 μM) was calculated vs. the intensity of untreated cells and normalized based on the intensity of respective β–Actin bands.

reticulum (ER) and mitochondria are closely linked within a very short distance, only a few nanometers (10–30 nm) apart, forming junctions where they are tethered together.[37,38] First, we delved into examining the potential impact of IrL¹ on the endoplasmic reticulum (ER), specifically focusing on its role in inducing ER stress. The Endoplasmic reticulum (ER) is the largest cell organelle which is mainly responsible for protein regulation, intracellular Ca^{2+} storage, and lipid biosynthesis.[39] Cell growth requires proper ER function, however, in cancer cells, the ER function becomes dysregulated resulting in increased ER stress in cancer cells. To cope with the ER stress, the unfolded protein response (UPR) pathway is upregulated by cancer cells, the mechanism by which cells control endoplasmic reticulum (ER) protein homeostasis. The UPR remains inactivated under normal conditions, however under stress conditions such as altered glycosylation or hypoxia, UPR gets activated because of the accumulation of unfolded proteins. UPR generally makes cancer cells resistant to chemotherapy.[40] Regardless of the UPR's role in developing cancer progression and resistance to chemotherapy, the chemical induction of ER stress has gained attention as an anticancer strategy. Such examples include the FDA-approved drugs carfilzomib and bortezomib, which induce ER stress by inhibiting the degradation of unfolded proteins. The UPR consists of three major pathways: PERK, IRE1, and ATF6.[41] IRE1, PERK, and ATF6 are the three ER transmembrane proteins that sense ER stress in the ER and become activated resulting in the regulation of a cascade of signaling pathways collectively termed as the Unfolded Protein Response (UPR). The main functions of UPR include the reduction of protein translation and activation of degradation of misfolded and unfolded proteins.[42] The cancer cell will survive if the UPR can mitigate the ER stress encountered by it. When the ER stress conditions are unresolvable then UPR fails to lower the ER stress and restore ER homeostasis and thus promote cell death.[43] In this study, we explored the impact of varying concentrations of IrL^1 on the activation of endoplasmic reticulum (ER) stress, specifically examining markers such as PERK and BiP through Western blot analysis. MDA-MB-231 cells were exposed to five doses of IrL^1, determined relative to the IC_{50} values obtained from the 48 h MTT experiment. The expression levels of ER markers were then compared to those of untreated cells, as illustrated in **Figure** 9a,b. Under non-stressful conditions, the endoplasmic reticulum (ER) chaperone, immunoglobulin binding protein (BiP), aids in protein folding by binding to protein kinase R-like ER kinase (PERK), preventing its activity. During the ER stress, the BiP protein dissociates from the PERK protein and the PERK protein undergoes autophosphorylation to form phospho-PERK. This is known as the PERK activation.[43a] The phosphorylation levels of PERK can be detected by the phospho-specific PERK antibody.[43b] Thus, during ER stress, the downregulation of PERK protein expression and upregulation of phospho-PERK protein expressions indicates PERK activation.[43c] In this western blot experiment we determined the expression of PERK protein and not the phospho-PERK protein. Therefore, we observed the PERK downregulation. The Western blot findings for PERK and BiP substantiated PERK activation, as the protein expression markedly decreased with escalating drug concentrations. For instance, at the highest drug dosage of 9 μμ, PERK intensity was approximately >90% lower than the control. Conversely, BiP intensity increased many folds compared to the control, indicating its dissociation from PERK and the initiation of the unfolded protein response (UPR).[44] Intense ER stress triggers the release of calcium ions (Ca^{2+}) from the endoplasmic reticulum (ER), stimulating the flux of Ca^{2+} between the ER and mitochondria, thereby leading to mitochondrial dysfunction.[45]

Consequently, we conducted a mitochondrial membrane potential assay. The impact of IrL^1 on the integrity of mitochondrial membrane potential was monitored by TMRM assay. The changes in the mitochondrial membrane potential (MMP) were detected by the fluorescence of the cells stained with TMRM (tetramethylrohdamine methyl ester) dye. The collapse in mitochondrial membrane potential was characterized by the reduction in red fluorescence of the dye in the positive control H_2O_2 and IrL^1 treated cells in comparison to the control. Figure 9c represents the concentration-dependent decrease in the red fluorescence. These results indicate that IrL^1 can cause the loss of MMP. The mitochondrial damage may result in the alteration of energy production pathways; therefore, we further explored the effect of IrL^1 on mitochondrial energy metabolism status, mainly the intracellular ATP level. As shown in Figure 9d IrL^1 treated cells represent the dose-dependent reduction in the intracellular ATP levels as compared to the control. Notably, ≈55% decrease in ATP production was found at the highest concentration of IrL^1 (200 μμ) when treated for 12 h. The combined results of MMP and ATP assay suggest that IrL^1 has the tendency to cause mitochondrial dysfunction and metabolic inhibition. Damage or impairment of mitochondria results in increased oxidative stress due to the generation of reactive oxygen species (ROS).[46a] Subsequently, we employed Mitosox, a probe specifically targeting mitochondrial superoxide ($O_2^{\bullet-}$), to assess this phenomenon. Figure 9e displays the significant increase in $O_2^{\bullet-}$ level treated with IrL^1.

2.13. Propensity Between Ferroptosis Induction and Organelle Targeting

To understand the precise mode of action between ferroptosis and organelle targeting further investigation was performed. Our previous experiments mentioned in the manuscript displayed that in the presence of Ferrostatin-1 (Fer-1), a known ferroptosis inhibitor, the cell viability of IrL^1 was enhanced, suggesting that ferroptosis was the cell death mechanism induced by IrL^1. To further investigate the propensity between ferroptosis induction and organelle targeting, the impact of co-incubation of IrL^1 with Fer-1 on mitochondrial function was evaluated. Results indicated that changes in mitochondrial membrane potential, mitosox staining, and ATP depletion still persisted as shown in the following Figures (Figures S54–S57, Supporting Information). The Fer-1 is unable to inhibit mitochondrial superoxide generation.[46b] These observations imply that while mitochondrial damage occurs, it is not the primary cause of cell death when ferroptosis is inhibited. This leads to the conclusion that IrL^1's targeting of mitochondria is insufficient to inhibit ferroptosis. Furthermore, previously, it was observed that increased cell viability of IrL^1 in the presence of NAC (an antioxidant), and enhanced lipid peroxidation observed by the C11-BODIPY probe, suggesting oxidative lipid damage as the mode of action of IrL^1. The inhibition of lipid peroxidation by Ferrostatin-1 is shown in Figure S56 (Supporting Information). It is reported that while lipid peroxidation in lysosomal or mitochondrial membranes can induce ferroptosis; the oxidative destruction of specific membrane lipids, particularly within the endoplasmic reticulum dominantly triggers the ferroptosis.[46c,d]

2.14. In-vitro and In-silico Intercalative Mode of Binding of IrL^1 with DNA

Considering the propensity of positively charged metal complexes possessing an extended aromatic surface to engage in

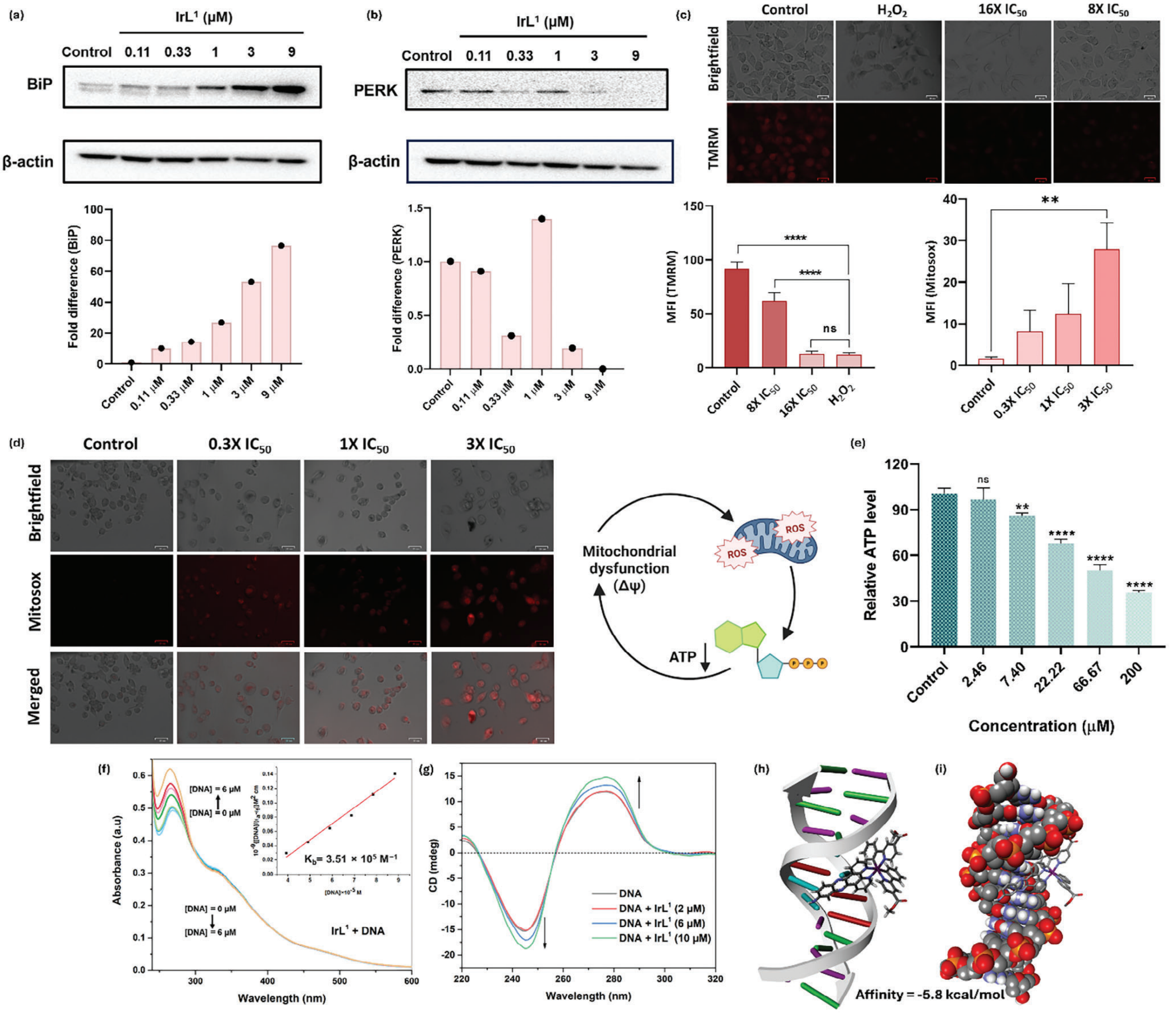

Figure 9. a,b) Analysis of various endoplasmic reticulum (ER) stress biomarkers by western blot. MDA-MB-231 cells were treated for 24 h with increasing concentrations of IrL^1 (0.11–9 μM). β-Actin was used as a loading control. The fold change in protein expression was calculated vs. the intensity of untreated cells and normalized based on the intensity of respective β–Actin bands. c) Change in Mitochondrial membrane potential ($\Delta\Psi_m$) observed by fluorescent images of TMRM dye-stained MDA-MB-231 cells after being incubated with IrL^1 for 0.5 h. The fluorescence was monitored by a BIO-RAD ZOE fluorescent cell imager. Untreated cells were taken as the negative control, and H_2O_2 was taken as the positive control. Scale bar: 25 μm. d) Mitosox assay for detection and quantification of superoxide in IrL^1-treated MDA-MB-231. Cells. Untreated cells were taken as the negative control. Scale bar: 25 μm. The fluorescence was monitored by a BIO-RAD ZOE fluorescent cell imager. The mean fluorescence intensity was calculated using Image J software. ****$p < 0.0001$, **$p < 0.01$, ns= non-significant. e) Decrease of cellular ATP levels in MDA-MB-231 cells incubated with IrL^1. Cells were treated with the indicated concentrations of IrL^1 for 12 h. The luminescence intensity was measured in a microplate reader. Untreated cells were taken as control. Each data point represents mean±SD, n =3. Significantly compared to control: ****$p < 0.0001$, **$p < 0.01$, ns= non-significant. Binding interaction of IrL^1 with CT-DNA in Tris-HCl buffer (pH=7.4) resulted in f) hyperchromism and isosbestic point in UV–vis titration studies of IrL^1 with CT-DNA. g) Circular dichroism (CD) spectra of CT-DNA with a fixed concentration of CT-DNA and increased concentrations of IrL^1 (2 μM- 10 μM). Inset f) Plot of $[DNA]/(\epsilon_a - \epsilon_f)$ vs. [DNA] for IrL^1. Molecular docking of IrL^1 with DNA (PDB: 1BNA) h) ribbon view i) space fill view.

non-covalent interactions with DNA,[47a] we speculated that nuclear/mitochondrial DNA could be among the potential targets of IrL^1. Owing to the compound's ability to intercalate with DNA and mitochondrial localization, both the nuclear and mitochondrial DNA can be suspected as the potential target. Indeed recently Ir(III) cyclometalated complexes have been reported to target mitochondrial DNA.[47b] Taking this into account we explored the interaction of IrL^1 with CT-DNA using UV–vis titrations study and Circular dichroism (CD) spectra. The UV–vis spectra shown in Figure 9f display a hyperchromic shift in π–π^* region and a hypochromic shift at the MLCT region that resulted in the appearance of an isosbestic point. These spectral

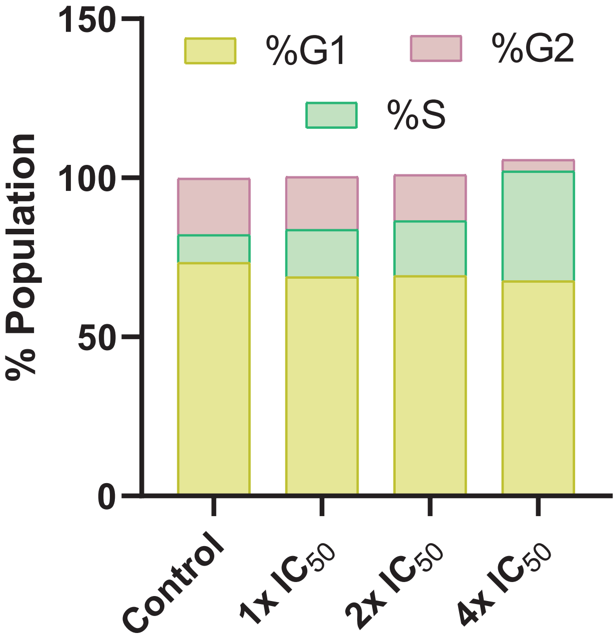

Figure 10. Cell cycle distribution of MDA-MB-231 cells treated with IrL^1 at indicated concentrations for 24 h. Untreated cells were taken as the control.

characteristics indicate the interaction of IrL^1 with DNA together through an intercalative mode of action.[20] The magnitude of the binding strength of IrL^1 with CT-DNA was calculated via the intrinsic binding constant $K_{b,}$ where $K_b = 3.51 \times 10^5$ M^{-1}. To confirm the results obtained by UV–vis, circular dichroism (CD) spectra were recorded. The positive band at 280 nm is due to left-handed helicity (due to the common arrangement of base stacking or nucleobases), while the negative band at 248 nm is due to the right-handed helicity of DNA. The changes in the CD signals of DNA upon interaction with the drug can be assigned to changes in the structure of DNA. The CD spectra obtained for CT-DNA and IrL^1 in Figure 9g resulted in substantial changes due to alterations in base stacking and helicity of DNA, indicating the intercalative mode of binding of IrL^1 with DNA.[48] To further evaluate the interaction of IrL^1 with DNA, computational modeling was performed using the optimized structure of IrL^1. The results obtained through docking also indicated the preferential intercalation of IrL^1 to B-DNA (Figure 9h,i).

2.15. Cell Cycle Disruption by IrL^1

To gain an insight into the effect of IrL^1 on cell cycle progression, the cell cycle arrest experiment on MDA-MB-231 cells was performed by flow cytometry. The cell cycle includes G0/G1, S, and G2/M phases, halting cell division at any of these phases leads to cell cycle arrest. As illustrated in **Figure 10** the percentage of cells at the S phase after treatment with IrL^1 at varying concentrations for 24 h, increased with concentration of IrL^1 from 14.9% (1X IC$_{50}$) to 34.5% (4X IC$_{50}$) compared to control (8.7%). These results suggest that IrL^1 induces cell cycle arrest during the S phase, a critical DNA synthesis period. In conclusion, IrL^1's ability to intercalate with DNA causes disruption in DNA replication that leads to S phase cell cycle arrest.

2.16. Synergistic Antitumor Effect of Cisplatin and by Combination Index (CI) and Isobologram Analysis

Combination therapy is being used for the management of many cancers as it offers the possibility of synergism between two drugs. Having the knowledge of a distinct mechanism of action of IrL^1 on cancer cells as compared to cisplatin, we explored the effect of both drugs on cancer cells when used in combination with each other. Following the previously reported protocol49, MDA-MB-231 cells were treated with IrL^1 and cisplatin in different ratios for 48 h. The cell viability was determined by MTT assay. As shown in **Figure 11a**, the IC$_{50}$ values obtained for different combinations of IrL^1 and cisplatin are considerably lower as compared to their IC$_{50}$ values alone. We utilized the combination index (CI) and isobologram methods to analyze whether the combination of these drugs resulted in synergistic, antagonistic, or additive effects. The following formula was used for calculating combination index (CI): $CI = C_A/C_{XA} + C_B/C_{XB}$, where C_A and C_B are the concentrations of drugs A and B required to achieve a certain effect using a combination of A and B, and C_{XA} and C_{XB} are the concentrations of drugs A and B alone. CI >1 implies antagonistic; CI = 1 implies additive; and CI < 1 implies synergistic effects.[50] As shown in Figure 11a, a strong synergistic effect was observed when IrL^1 and cisplatin were used in a 2:1 ratio whereas the antagonistic effect was observed at other ratios. To verify these results the experiment was repeated in triplicates in a set of three independent experiments. Next, we generated the isolobogram by plotting the IC$_{50}$/48 h values obtained for individual agents and for combinations. As shown in Figure 11b, the isolobogram also showed the synergistic antitumor effect of cisplatin and IrL^1, which is consistent with our analysis using CI values.

2.17. Intracellular Distribution of IrL^1 within 3D-Multicellular Spheroids (MCTSs)

In drug delivery, it is essential to ensure prolonged circulation in the bloodstream and efficient penetration into deep tumor regions, aspects directly impacted by the size and structure of nanomaterials. Considering the necessity for deep tumor penetration, multicellular spheroids (MCTSs) of MDA-MB-231 cells with a diameter of 500–600 µm were developed. MCTSs are characterized by multilayered cell structures that show diffusional limits to drug penetration and MCTSs also develop the hypoxic core which can make the tumor cells resistant to cancer therapeutics.[51,52a] The 3D MDA-MB-231 spheroids were treated with varying concentrations of IrL^1. Figure 11c shows the diffusion efficacy of IrL^1 nanoaggregates into the tumor spheroids. The IrL^1 treated spheroids collapsed remarkably upon photoirradiation (390 nm, 0.363 mW cm^{-2}, 25 min) showing a higher photodynamic effect compared to the dark conditions. The loss of integrity in treated spheroids in the dark and via photoirradiation compared to control indicated the potential of IrL^1 nanoaggregates to suppress hypoxic 3D solid tumors.

(a)

Cisplatin : IrL^1 (ratio)	1:1	1:2	1:4	1:8	2:1	4:1	8:1	Single agent
				IC$_{50}$ values (μM, 48 h)				
Cisplatin	0.40	1.21	3.7	4.32	0.04	0.1	0.14	5.29
IrL^1	0.40	0.60	0.93	0.54	0.08	0.4	1.12	0.33
Combination Index (CI)	1.29	2.04	3.51	2.45	0.25	1.23	3.42	-
	Antagonistic	Antagonistic	Antagonistic	Antagonistic	Synergistic	Antagonistic	Antagonistic	

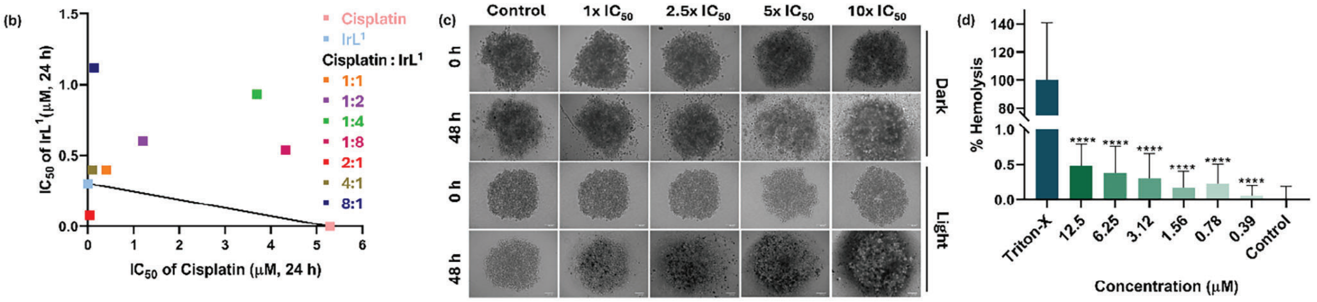

Figure 11. a) IC$_{50/48h}$ values (μM) and CI values in MDA-MB-231 cells for cisplatin and IrL^1 when used as a single agent or in combinations (48 h incubation MTT assay). b) Isobologram of cisplatin and IrL^1 in MDA-MB-231 cells. c) Microscopic images of MDA-MB-231 Multicellular tumor spheroids (MCTSs). MCTSs were treated with different concentrations of IrL^1 with respect to IC$_{50}$ obtained in 2D culture for 48 h. Photoirradiation was conducted by an LED light of 390 nm (0.363 mW/cm^2, 25 min). The images for 0 h were recorded before treatment. Scale bar: 100 μm. d) Hemolytic activity of IrL^1 on human RBCs. 0.1% Triton X-100 was used as the positive control. Each data point represents mean ± SD, n =3. Significantly compared to positive control: ****$p < 0.0001$.

2.18. Hemolysis Evaluation of IrL^1

Prior to exploring the translational potential of our compound through in-vivo experiments, it is imperative to ensure the safety and efficacy of the drug candidates. We focused on understanding the impact of IrL^1, a potential therapeutic agent, on mammalian cells, particularly red blood cells (RBCs). Through meticulous examination across a spectrum of concentrations, ranging from 12.5 to 0.39 μμ, we meticulously evaluated IrL^1's hemolytic potential. Our findings reveal that IrL^1 demonstrates remarkable biocompatibility, with minimal hemolysis observed, even at higher concentrations, measuring ≤1%. Intriguingly, within its IC$_{50}$ range, IrL^1 showcases non-hemolytic behavior, with hemolysis rates below 0.5% (Figure 11d). These results underscore the promising safety profile of IrL^1, positioning it as a potentially viable therapeutic option. 0.1% Triton X-100, a positive control, elicited complete hemolysis.

2.19. IrL^1 Therapeutic Efficacy In vivo

The safety and efficacy of IrL^1 in blood further prompted us to explore the therapeutic efficacy of IrL^1 4T1 xenograft NOD.CB17-Prkdcscid/NCrCrl mice. After 4T1 tumor establishment, the mice were randomly divided into two groups of four mice each, i.e., control, and drug-treated. The schematic in **Figure 12a** outlines the experimental details.

The body weight and tumor volume of each mice were monitored every two days a week revealing high biocompatibility of IrL^1 as mice did not lose any weight compared to control during the treatment (Figure 12b). After 16 days of treatment, all mice were euthanized, blood and all major organs (heart, liver, spleen, kidney, intestine, and lung) and tumor were harvested, and the tissues were examined by hematoxylin-eosin (H & E) staining. The photographs of the harvested tumor are represented in Figure 12e. The inductively coupled mass spectrometry (ICP-MS) data (Figure 12f) illustrates that IrL^1 was accumulated majorly in the spleen of mice whereas the H & E staining indicates no injuries or abnormalities in any organs including the spleen (Figure 12m). On the other hand, significant damage was observed in IrL^1-treated tumor tissue compared to the control. The morphological analysis of erythrocytes indicates no toxicity of IrL^1 on the erythrocytes (Figure 12g). The complete blood count is shown in Figure 12h–l. Figure 12c,d illustrates the reduction in tumor volume in IrL^1-treated mice compared to control. The above indices indicate the safety and efficacy of IrL^1 in mice models.

3. Conclusion

In summary, this research outlines the synthesis of a novel set of organometallic Ir(III) complexes, incorporating COOMe groups to augment cellular permeability. Notably, the lead compound, IrL^1, exhibits the formation of nanoaggregates within cell culture media, thereby facilitating enhanced diffusion in deep-seated tissue within 3D MDA-MB-231 tumor spheroids. Under 390 nm light exposure IrL^1 exhibited remarkable photocytotoxicity with an IC$_{50}$ value of 36.05 ± 0.03 nM and exhibited a more pronounced effect on 3D MDA-MB-231 spheroids compared to dark conditions. Upon internalization via energy-dependent endocytosis, IrL^1 selectively targets the endoplasmic reticulum and mitochondria, showcasing potent anti-tumor properties through ferroptosis-mediated cell death, ER stress induction, mitochondrial dysfunction, and DNA intercalation. Importantly, IrL^1

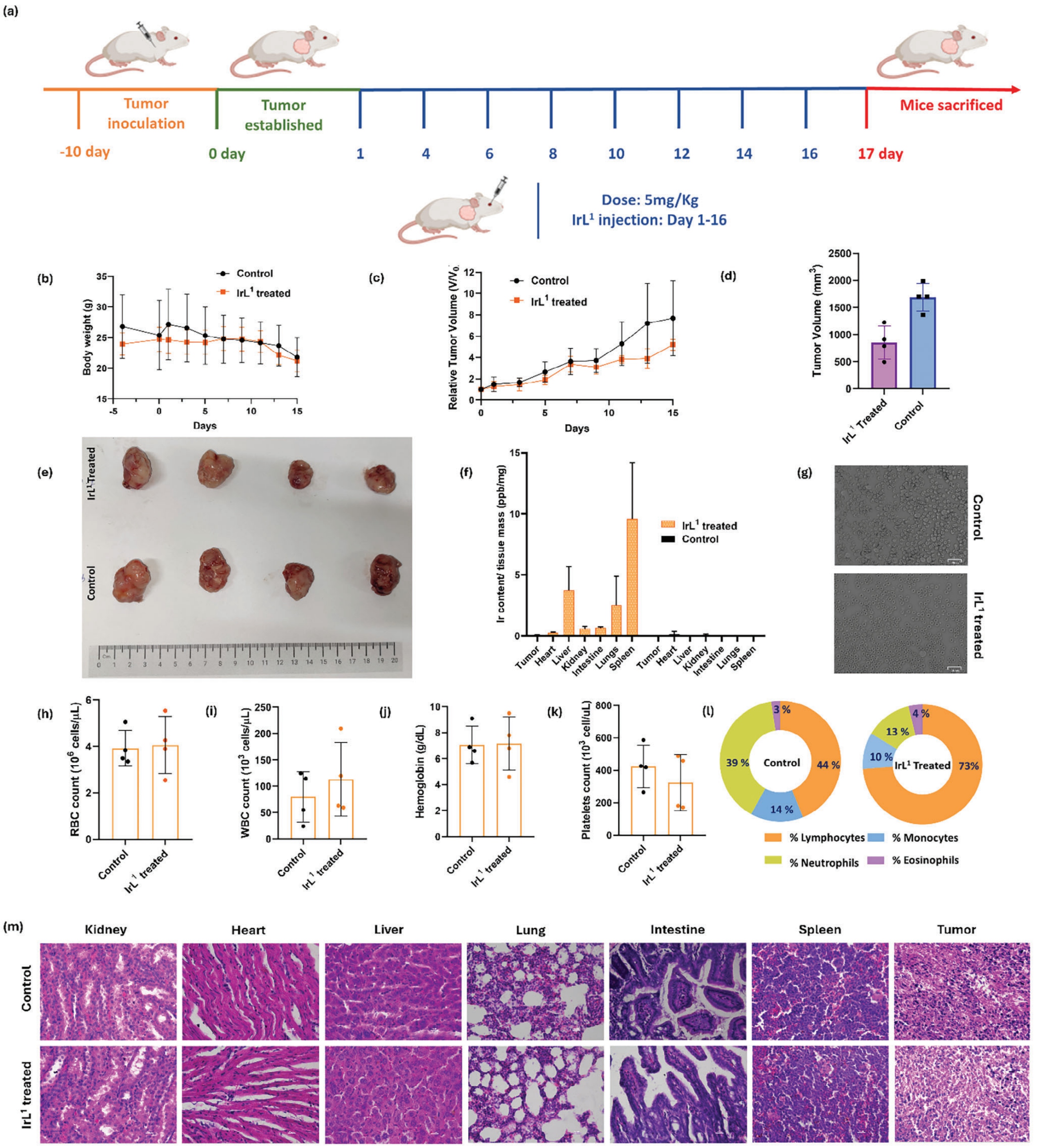

Figure 12. In vivo antitumor efficacy of IrL^1 in 4T1 tumor-bearing NOD.CB17-Prkdcscid/NCrCrl mice. a) Schematic detail of the treatment. b) Body weight of the animals during treatment. c) Relative tumor volume during the treatment period. d) Tumor volume post-treatment e) Photographs of the tumor harvested after 16 days of treatment. f) Biodistribution of IrL^1 after 16 days of treatment. g) Erythrocyte images h) RBC count i) WBC count j) Hemoglobin k) Platelets count from the blood collected after euthanization. l) Percentage of lymphocytes, monocytes, neutrophils, and eosinophils in the blood collected from control and IrL^1-treated mice. m) Histological examination of different organs with hematoxylin and eosin (H & E) stain from the tissues harvested after euthanization.

demonstrates minimal hemolytic activity, indicating a favorable safety profile for therapeutic utilization. The Ir(III) complexes existing in the literature for the treatment of TNBC displayed limited cytotoxicity compared to IrL^1 both in dark and light conditions. Uniquely, IrL^1 nanoaggregates induce ferroptosis-mediated cell death and cause mitochondrial dysfunction and ER stress generation. The similar existing Ir(III) complexes in the literature induce ferroptosis-mediated cell death by multiple pathways such as ferroptosis-apoptosis, ferroptosis-autophagy, and ferroptosis-pyroptosis pathways.[52b–e] The reported molecules that specifically induce ferroptosis were incorporated with the ferroptosis-causing agents in their such RSL3 and ferrocene,[52f,g] whereas IrL^1 specifically induces ferroptosis only and without the incorporation of ferroptosis-inducing agents in its structure. Furthermore, IrL^1 exhibits low hemolysis in blood, indicating a high level of safety. Notably, no other ferroptosis-inducing molecules reported to date possess the distinctive capability to undergo nanoaggregation, a novel feature that enhances therapeutic specificity and effectiveness, particularly against MDA-MB-231 cells. This combination of selective ferroptosis induction among other cell death pathways along with its safety and unique nanoaggregation property, underscores the novelty and significance of IrL^1 compared to the existing molecules.

Collectively, the utilization of nanoaggregates comprising organometallic Ir(III) complexes, as corroborated by comprehensive in vitro, in silico, and in vivo analyses, presents a promising strategy for enhancing delivery efficiency and achieving profound tumor penetration, particularly in the context of challenging triple-negative breast cancer. Consequently, this work unveils a novel Ir(III) complex with exceptional properties to form nanoaggregates that can act as photodynamic therapy (PDT) agents, suggesting a new promising strategy for its future study to elucidate its mode of action under light exposure. Future structural refinements hold the potential for diversifying the repertoire of organometallic Ir(III) nanoaggregates with adaptable characteristics, thereby advancing their clinical applications within the realm of oncology and the field of nanomedicine.

4. Experimental Section

Synthesis of C^N Ligands: To a solution of 2-Bromo-isonicotinic acid (1eq.) and boronic acid (1.2 eq.) in THF: Water (3:5) was added K_2CO_3 (3.0 eq.) and the reaction mixture was stirred until both the reactants had dissolved completely. Then $Pd(PPh_3)_2Cl_2$ (0.05 eq.) was added, and the reaction mixture was heated to 70 °C for 24 h. After the reaction completion, the reaction mixture was filtered, THF was evaporated, and the remaining solution was extracted with DCM. The aqueous layer was acidified with 1 M citric acid to pH 3 to get the precipitates. The precipitates were dried to get the product. To the round bottom flask equipped with a magnetic stirrer was added the product obtained (1 eq.) and dry MeOH (10 eq.). To this was then added conc. H_2SO_4 (0.2 eq.) and the reaction mixture was refluxed for 8 h. Reaction completion was monitored by TLC. After reaction completion, the solvent was evaporated, and the reaction mixture was extracted with DCM and saturated sodium bicarbonate solution and concentrated to dryness to get the final product.

Synthesis of N^N Ligand: The ligand dipyrido[3,2-a:2′,3′-c]phenazin-11-amine (adppz) was prepared according to the reported method.[53]

Synthesis of $[(C\hat{}N)_4Ir_2Cl_2]$: To the microwave vial equipped with a magnetic stirrer was added the (C^N) ligand (2 eq.) and $IrCl_3.xH_2O$ (1 eq.). The solvent ethylene glycol: water (4:1) 5 mL was added, and the reaction mixture was subject to microwave radiation for 60 min at 120 °C or refluxed at 120 °C for 24 h. The red precipitates obtained were then filtered, washed with water and diethyl ether, and dried. Yield: 75–80%. The formation of the intermediates was characterized by ESI-MS and the next step proceeded without any further purification.

Synthesis of IrL$^{1-8}$: A mixture of $[(C\hat{}N)_4Ir_2Cl_2]$ (1 eq.) and (N^N) ligand (2.2 eq.) in DCM: MeOH (1:1, v/v %) was refluxed under for 12 h. The solution was cooled down to room temperature and then NH_4PF_6 (10 eq.) was added to it. The reaction mixture was stirred for the next 3 h at room temperature and then filtered. The filtrate was concentrated to dryness. The product obtained was purified by silica gel column chromatography in acetone/DCM.

Purity Analysis of Ir(III) Complexes: The RP-HPLC analysis was utilized to determine the purity of IrL^1-IrL^1 complexes. For this, the solution of the complexes in 20/80 (v/v) acetonitrile/water was injected into the RP-HPLC column. The detection wavelength was set as 254 nm. HPLC-grade acetonitrile and MQ water containing 0.1% TFA v/v were used as the mobile phase in the experiment.

Photophysical Properties in Solution: UV–visible absorption spectra were obtained on a JASCO V-770 UV–visible–NIR spectrophotometer equipped at room temperature. All the photoluminescence spectra were recorded on HORIBA Fluromax-4 at room temperature. Stock solutions of the compounds were prepared in DMSO. Photoluminescence quantum yields (Φ_{em} or PLQYs) in solution were obtained from corrected spectra and measured according using fluorescein ($\Phi = 0.79$, in 0.1 M NaOH) as standard. The quantum yield calculations were done using the equation: $\Phi = \Phi_{ref} \times (A_{ref}/A) \times (I/I_{ref})$.

Stability of Ir(III) complexes by UV–vis Absorption Spectroscopy: The stability of Ir(III) complexes was investigated by UV–vis absorption spectroscopy in tris buffer (pH = 7.4) as solvent. Briefly, the Ir(III) complexes were dissolved in DMSO and the absorption spectra were recorded in tris buffer for 0, 24, and 48 h at room temperature.

Lipophilicity by ICP-MS: The flask-shaking method and ICP-MS analysis were utilized to determine the lipophilicity (log $P_{o/w}$) of Ir(III) complexes. An equivalent amount of 0.9% (w/v) NaCl solution, saturated with octanol, was introduced into a 1 mL stock solution of the Ir(III) complexes in n-octanol. The resulting mixture was agitated for 24 h in an incubator set at 37 °C. Following this, the mixtures underwent centrifugation at 4000 × rpm for 10 min. Subsequently, the distinct oil and water phases were carefully isolated. A total of 100 µL from each of the oil and water phases were subjected to dissolution using 65% HNO_3 (300 µL) and subsequently diluted to a final volume of 10 mL using distilled water. The concentration of Ir(III) (C_o or C_w) was determined via the ICP-MS technique utilizing an internal reference. The $P_o/_w$ value is directly proportional to the ratio of the concentration of the organic phase (C_o) to the attention of the aqueous phase (C_w).

Cell Lines and Cell Culture Conditions: Breast adenocarcinoma cell lines MDA-MB-231 and MCF-7, Human lung adenocarcinoma cell line A549, Human colon cancer cell line HCT-116, Human embryonic kidney cell line HEK-293, and Human prostate cancer cell line PC3 was obtained from National Centre for Cell Science (NCCS Pune, India). The cell lines were maintained in RPMI 1640 (MDA-MB-231, MCF-7, A549, and PC3) or DMEM medium (HCT-116, HEK-293), supplemented with 10% fetal bovine serum, 100 Units mL^{-1} penicillin and 100 µg mL^{-1} streptomycin, at 37 °C humidified atmosphere with 5% CO_2. All stock solutions of the compound were prepared in DMSO.

MTT Assay: The cytotoxicity of the compounds was determined by the MTT assay. For each cell type, 0.35×10^6 cells were plated in a culture flask. The cells were harvested from culture flasks by trypsinization and seeded into 96-well microculture plates at the seeding density of 2500 cells per well. After the cells were allowed to resume exponential growth for 24 h, they were exposed to drugs at different concentrations in media for 48 h. Cisplatin (10 µµ) and untreated cells were used as positive and negative controls, respectively. After the exposure of 44 h, the cells were treated with MTT solution (100 µLeach well, 5 mg mL^{-1}) for 4 h in the dark, and then absorbance was measured at 570 nm by SpectraMax M5^e microplate reader. The photocytotoxicity was carried out by using Kessil PR160 LED 390 nm, 0.363 mW cm^{-2} at a height of 60 cm. All procedures were carried out in a triplicate of three independent experiments. IC$_{50}$ values were calculated using GraphPad Prism software and the results were presented as a mean ± SD.

Cellular Uptake by ICP-MS: MDA-MB-231 cells were plated in a 6-well plate (1×10^6 cells each well). After 24 h incubation, the medium was replaced by a medium containing IrL^1 and $IrCl_3.xH_2O$. After 8 h incubation, the culture medium was aspirated. Cells were trypsinized, counted, and washed three times with PBS. Then, cells were centrifuged at 3000 rpm at 4 °C for 10 min, and digested in HNO_3 for two days. Each sample was diluted to 10 mL before the test. The amount of Ir in cells was determined by ICP-MS. The experiment was performed in triplicates.

Physiochemical Characterizations of Nanoaggregates: Dynamic light scattering (DLS) was conducted at room temperature on a Zetasizer Nano ZS90 by Malvern. Scanning electron microscopy (SEM) and energy dispersive X-ray spectroscopy (EDS) elemental mapping images were taken on a Zeiss scanning electron microscope. High-resolution TEM (HRTEM) was conducted on FEI-Titan G2 60–300 KV TEM.

Multicellular Tumor Spheroids (MCTSs) Formation: The spheroids were cultured in 96-well plates coated with 1.5% agarose. 2500 cells each well were seeded per well and the spheroids were maintained in a humidified cell culture incubator at 37 °C with a 5% CO_2 atmosphere. The integrity of spheroids after treatment with IrL^1 was monitored by a BIO-RAD ZOE microscope. The spheroids were irradiated by using Kessil PR160 LED 390 nm, 0.363 mW cm^{-2} at a height of 60 cm.

Cellular Uptake Mechanism: MDA-MB-231 cells were stained with IrL^1 complex under different conditions by varying the temperature (4 and 37 °C) as well as pretreated with metabolic inhibitor (CCCP) and endocytic inhibitors (chloroquine and NH_4Cl). The cells were observed under a BIO-RAD ZOE fluorescent cell imager to determine the cellular uptake by their fluorescence.

Intracellular Localization: The MDA-MB-231 cells were incubated with IrL^1 (3.3 μM) at 37 °C for 3 h and then co-incubated with ER-Tracker Red (1 μM), MitoTracker Deep Red FM (500 nM), or LysoTracker Deep Red DND-26 (50 nM) at 37 °C for 0.5 h, then washed by PBS three times. Cells were then immediately visualized by fluorescent microscope. The excitation wavelength for IrL^1 was 460 nm, while the excitation wavelengths of ER-Tracker Red, LysoTracker Deep Red DND-26, and MitoTracker Deep Red FM are 587, 647, and 644 nm. Emission filter:(peak wavelength of IrL^1) ± 20 nm respectively, and 615 ± 20 nm for ER-Tracker Red, 668 ± 20 nm LysoTracker Deep Red DND-26, and 665 ± 20 nm for MitoTracker Deep Red FM.

Determination of Mechanism of Cell Death in Presence of Inhibitors: The cell viability of MDA-MB-231 cells was measured by MTT assay after 24 h co-culture with a variety of inhibitors and IrL^1 complex. MDA-MB-231 cells were seeded in a 96-well plate, with 2500 cells each well. Cells were allowed to adhere overnight. The cells were then pre-incubated for 30 min with the inhibitors Z-VADfmk (15 μM), 3-methyladenine (100 μM), cycloheximide (0.1 μM), Necrostatin-1 (50 μM), CCCP (40 μM), Ferrostatin-1 (50 μM) and NAC (1 mM) which. IrL^1 was then incubated in the concentration of 0.8, 1.6, 3.12, and 6.25 μM for 24 h. Cisplatin was incubated at the concentration of 5.3, 10.6, and 21.2 μM for 24 h. MTT assay was then performed to determine the % cell viability in the presence of these inhibitors.

Electrochemical Profile: The electrochemical experiment was carried out with the CHI610E electrochemical analyzer. Cyclic voltammetry was performed under an N_2 atmosphere at room temperature using a cell equipped with three electrodes: glassy carbon as the working electrode, platinum wire as the counter electrode, and the $Ag/AgNO_3$ (0.01 M in CH_3CN) as the reference electrode. The measurement was performed in dry CH_3CN solutions with 0.1 M tetrabutylammonium perchlorate [nBu$_4$N] [ClO_4] as the supporting electrolyte, with 1 mM of the compound to be investigated in it at a scan rate of 100 mV S^{-1}. The potential values were reported versus the potential of the Ag/Ag^+ couple used as a reference.

ROS Generation in Cells: MDA-MB-231 cells (2.5×10^4 cells each well) were seeded in 96 well plates and allowed to adhere overnight. Afterward, one set of the cells was pretreated with N-acetyl cysteine (1 mM) for 1 h. After 1 h both sets, with and without N-acetyl cysteine were treated with different concentrations of IrL^1. Hydrogen peroxide (H_2O_2) was used as a positive control whereas untreated cells were used as a negative control. After 3 h of incubation, the media was removed, and the cells were washed with 1X PBS. Then, a solution of 2′,7′-dichlorodihydrofluorescein diacetate (H_2DCF-DA; 10 μM, 100 μL) in 1X PBS was added to the cells and incubated in the dark at 37 °C for 30 min. The cells were then washed thrice with 1X PBS to remove excess H_2DCF-DA. Fluorescent images were captured immediately using a BIO-RAD ZOE fluorescent cell imager.

Lipid Peroxidation Assay: MCF-7 cells (2.5×10^4 cells each well) were plated in 96 well plates and allowed to adhere overnight. Afterward, the cells were treated with Ir(III) complex IrL^1 with its two-fold dilutions. Untreated cells were used as a negative control in this experiment. After 3 h of incubation, the media containing compounds was removed and the cells were washed with PBS. Then, a solution of C11-BODIPY (2.5 μm) in media was added to the cells and incubated in the dark at 37 °C for 30 min. The cells were then washed thrice with PBS to remove excess C11-BODIPY and fluorescence microscopy images were captured immediately using a BIO-RAD ZOE fluorescent cell imager. Following the same protocol, fluorescence detection was also performed by the FL-1H channel on a flow cytometer (BD FACSCalibur).

Intracellular Glutathione Depletion Assay: The GSH-Glo Glutathione Assay is a luminescence-based assay for detecting and quantifying glutathione (GSH). The experiment was performed according to the assay protocol. In the 96-well plate, 2500 MDA-MB-231 cells were seeded and allowed to adhere overnight. The cells were treated with different concentrations of IrL^1 and incubated for 24 h. Afterward, the media was aspirated, and cells of each well were treated with 100 μL of prepared 1X GSH-Glo Reagent and incubated for 30 min at room temperature. Furthermore, 100 μL of reconstituted Luciferin Detection Reagent was added to each well and incubated for 15 min. The luminescence was then recorded using a plate reader.

Western Blot: MDA-MB-231 cells (1×10^6) were seeded in a 6-well plate. After overnight incubation, the cells were treated with increasing concentrations of IrL^1 (0.11–9 μM) for 24 h. After 24 h treatment, the cells were washed with 1X PBS and lysed using the lamellae buffer. The cell lysates were scraped, collected, and stored at 4 °C. The protein concentration for each sample was measured by Bradford assay. Samples with the same protein concentration (20 μg) were heated at 100 °C for 5 min. The protein mixtures were separated on SDS-PAGE gel (12%) and then transferred to the PVDF membrane. The membrane was blocked with 5% skimmed milk for 2 h and then incubated with the primary antibodies overnight at 4 °C. The samples were also incubated with β-actin antibody as a loading control. The membranes were washed with 1X TBST thrice (5 min each) and incubated for 2 h with the secondary antibody. After incubation, the membranes were again washed thrice with 1X TBST (5 min each) and visualized using SuperSignal West Pico Plus Chemiluminescent substrate and a chemiluminescence imaging machine (ChemiDoc Touch imaging system, BioRad). The fold change in each protein expression was analyzed using Image J software.

TMRM assay: MDA-MB-231 cells (1.5×10^4 cells each well) were plated in 96 well plates and allowed to adhere overnight. Afterward, the cells were treated with Ir(III) complexes. Hydrogen peroxide (H_2O_2 150 μM) was used as a positive control whereas untreated cells were used as a negative control in this experiment. After 3 h of incubation, the media containing compounds was removed and the cells were washed with PBS. Then, a solution of tetramethyl rhodamine methyl ester perchlorate (TMRM; 50 nM, 100 μL) in RPMI-1640 media was added to the cells and incubated in the dark at 37 °C for 30 min. The cells were then washed thrice to remove excess TMRM and fluorescence microscopy images were captured immediately using a BIO-RAD ZOE fluorescent cell imager.

ATP Assay: ATP production was measured using the Cell Titer-Glo luminescence cell viability assay kit (Promega) according to the manufacturer's instructions. MDA-MB-231 cells were cultured in an opaque-walled 96-well plate and treated with IrL^1 at the indicated concentrations for 12 h. 100 μL Cell Titer-Glo reagent was added to each well. The plate was incubated at room temperature for 30 min. Luminescence intensity was measured in a microplate reader.

Mitosox Staining: To detect superoxide radicals, 2.5×10^4 MDA-MB-231 cells were seeded on the 96-well plate for 24 h. After 24 h the cells were then treated with different concentrations of IrL^1 for 3 h. The cells were then washed with 1X PBS and incubated with 1 μм mitosox (M36007) for 30 min at 37 °C. The cells were then washed thrice with to remove excess Mitosox and fluorescence microscopy images were captured immediately using a BIO-RAD ZOE fluorescent cell imager. The mean fluorescence intensity was calculated by Image J software.

DNA Binding Studies: The binding of IrL^1 with CT-DNA was examined via UV–vis absorption titrations and CD spectroscopy. The stock solution of CT-DNA was prepared in tris buffer (pH = 7.4). The DNA concentration was monitored by UV absorption measurements using $\epsilon_{260\ nm} = 6600\ M^{-1}\ cm^{-1}$. The titration study was performed by maintaining the concentration of IrL^1 (8.6 μμ) constant and increasing the concentration of CT-DNA from 0 to 6 μμ. The absorbance was measured 10 min after the addition of CT-DNA. The intrinsic binding constant (K_b) of IrL^1 with CT-DNA was determined by using the equation: $[DNA]/(\epsilon_a - \epsilon_f) = [DNA]/\ (\epsilon_b - \epsilon_f) + 1/K_b\ (\epsilon_b - \epsilon_f)$, where ϵ_a is the extinction coefficient of the complex at a given DNA concentration, ϵ_b is the extinction coefficient of complex when fully bound to DNA, ϵ_f is the extinction coefficient of the complex in free solution. The plot $[DNA]/(\epsilon_a - \epsilon_f)$ versus [DNA] gave the slope $1/\ (\epsilon_b - \epsilon_f)$ and intercept $1/\ K_b\ (\epsilon_b - \epsilon_f)$, K_b was calculated as the ratio of slope to intercept. The CD spectra of solutions were measured after 2 h incubation of compounds at room temperature in the range from 220 to 320 nm on a JASCOJ-1500 spectrometer. The concentration of CT-DNA was fixed and that of IrL^1 was varied from 2 to 10 μμ.

Cell-Cycle Disruption: MDA-MB-231 cells were seeded at a density of 10^6 cells each well in a 6-well plate. After 24 h incubation, the cells were treated with different concentrations of IrL^1 for 24 h. After 24 h the samples were harvested, washed with 1X PBS, fixed with 70% ethanol, and kept at 4 °C overnight. Fixed cells were washed with 1X PBS and stained with propidium iodide (20 μg mL^{-1}) and 100 μg mL^{-1} RNase A for 30 min at 37 °C. The cell cycle profile was measured by a flow cytometer. The analysis was performed by Flow Jo software using the Dean–Jett–fox method.

Structure Optimization and Molecular Docking: The complexes were optimized in the gas phase by DFT (Density Functional Theory)[54–56] using Gaussian 16.[57] Calculations were performed using B3LYP functional along with 6–31G** basis set for C, H, N, O while LANL2DZ was used for Ir with effective core pseudopotential of the metal.[58–60] The optimized structure of IrL^1 was docked to DNA dodecamer structure (PDB: 1BNA)[61] using Autodock, version 1.5.7. Binding poses were viewed by Discovery Studio software.

Cisplatin and IrL^1 Combination Study: In a 96-well plate, MDA-MB-231 cells were seeded at a density of 2500 cells per well and incubated for 24 h. Stock solutions of IrL^1 and cisplatin were serially diluted in a culture medium. The cells were then treated with different concentrations of IrL^1 and cisplatin in the following ratio (IrL^1: Cisplatin): 1:1, 1:2, 2:1, 1:4, 4:1, 1:8, and 8:1. The plate was then incubated for 48 h. The % cell viability was determined by performing an MTT assay. The experiment was performed in triplicates in a set of three independent experiments.

Hemolytic Assay: To investigate the induction of hemolysis by IrL^1, fresh human blood was used in this experiment. Briefly, the blood was collected and centrifuged at 1500 rpm for 10 min to remove blood plasma. The pellet of red blood cells (RBCs) were then washed thrice in PBS. Afterward, RBCs were resuspended in 4% v/v in the PBS buffer. Compound IrL^1 was dissolved in DMSO and serially diluted. In the 96-well plate, 20 μL of each concentration was added to the 100 μL of RBC suspension in each well, and a volume of 200 μL was achieved by adding PBS. The plate was immediately kept for the incubation of 1 h. After incubation, the plates were centrifuged again at 1500 rpm for 10 min, the supernatant (20 μL) was added to 80 μL of PBS in a fresh 96-well plate and hemoglobin release was measured. The optical density (OD) at 414 nm was measured for the hemoglobin release by using a SpectraMax $M5^e$ microplate reader. For positive control, 0.1% Triton X-100 was used whereas untreated RBC suspension was used as negative control. Percentage hemolysis was calculated using the formula:

$$\%\ \text{Hemolysis} = [(\text{OD of Sample} - \text{OD of untreated cells})/ \\ (\text{OD of Triton X} - \text{OD of untreated cells})] \times 100 \qquad (1)$$

In vivo Therapeutic Evaluation: The animal experimental protocols were approved by the Institutional Animal Ethics Committee (IAEC) of the Indian Institute of Technology Kanpur with an approval number IEC Communication Number: IITK/IEC/2023-24/I/10 and: lITK/IAEC/2023/1186. Eight-week-old female NOD/SCID mice were purchased from Hylasco Biotechnology (India) Pvt. Ltd. Hyderabad. After ≈10 days of inoculation, the 4T1 cells were injected subcutaneously into the right flanks of mice. After tumor establishment (day 0), mice were randomly divided into two groups of four mice each. The control group (saline-treated) and the IrL^1-treated group were intravenously injected with saline (100 μL) and IrL^1 (5 mg Kg^{-1} dose, 100 μL). The first dose was recorded as day 1. The body weight, length, and width of tumors were recorded every second day. The tumor volume was calculated by the formula 0.5 × length × (width)2. On the 17th day, the mice were sacrificed, the blood was collected, and the morphology of erythrocytes were captured. The tumors were stripped out for photograph and weight. Other organs (heart, liver, kidney, lungs, intestine, and spleen) were also harvested and fixed in 4% paraformaldehyde for H & E staining. The organs were digested in aqua regia to determine the Ir content by ICP-MS.

Supporting Information

Supporting Information is available from the Wiley Online Library or from the author.

Acknowledgements

The authors express their gratitude to Madhu Verma (Prof. Sri Sivakumar's laboratory), for granting access to the flow cytometer instrument. The authors are thankful to Prof. S. Ganesh's laboratory (BSBE department, IITK) for granting access to the plate reader (SpectraMax M5) and ChemiDoc. The authors are also thankful to Prof. Sandeep Verma's Lab (Chemistry Department, IITK) for granting access to the HPLC instrument. This work was supported by the DST SERB Start-up Research Grant (Grant 2021435), INSPIRE Faculty Research Grant (Grant 2019295), and Prime Minister Research Grant (PMRF-ID: 2300572).

Conflict of Interest

The authors declare no conflict of interest.

Author Contributions

The manuscript was written through the contributions of all authors. All authors have given approval to the final version of the manuscript. A.C., N.S., R.P., and S.D. executed the synthesis. A.C. executed all characterizations. N.S. performed and analyzed the CV experiment. A.C. and A.K. worked on all mammalian cell-based experiments and molecular docking studies. A.C., A.K., and K.C. worked on in-vivo experiments. A.C. executed DFT studies. H.S. analyzed the X-ray structures. The authors declare no competing financial interest.

Data Availability Statement

The data that support the findings of this study are available from the corresponding author upon reasonable request.

Keywords

ferroptosis, iridium, photoresponsive, triple negative breast cancer, tumor

Received: August 7, 2024
Revised: October 23, 2024

[1] J. Choi, J. S Koo, *Histol. Histopathol.* **2012**, *27*, 1481.

[2] M. Liao, J. Zhang, G. Wang, L. Wang, J. Liu, L. Ouyang, B. Liu, *J. Med. Chem.* **2021**, *64*, 2382.

[3] R. Mahmoud, P. Ordóñez-Morán, C. Allegrucci, *Cancers (Basel)* **2022**, *14*, 4280.

[4] L. Yin, J. J. Duan, X. W. Bian, S. C. Yu, *Breast Cancer Res.* **2020**, *22*, 61.

[5] A. Goldhirsch, E. P. Winer, A. S. Coates, R. D. Gelber, M. Piccart-Gebhart, B. Thürlimann, H. J. Senn, K. S. Albain, F. André, J. Bergh, H. Bonnefoi, D. Bretel-Morales, H. Burstein, F. Cardoso, M. Castiglione-Gertsch, A. S. Coates, M. Colleoni, A. Costa, G. Curigliano, N. E. Davidson, A. Di Leo, B. Ejlertsen, J. F. Forbes, R. D. Gelber, M. Gnant, A. Goldhirsch, P. Goodwin, P. E. Goss, J. R. Harris, D. F. Hayes, et al., *Ann. Oncol.* **2013**, *24*, 2206.

[6] M. Colleoni, N. Rotmensz, C. Robertson, L. Orlando, G. Viale, G. Renne, A. Luini, P. Veronesi, M. Intra, R. Orecchia, G. Catalano, V. Galimberti, F. Nolé, G. Martinelli, A. Goldhirsch, *Ann. Oncol.* **2002**, *13*, 273.

[7] R. L. Siegel, K. D. Miller, A. C S Jemal, *CA Cancer J. Clin.* **2019**, *69*, 7.

[8] G. Bianchini, J. M. Balko, I. A. Mayer, M. E. Sanders, L. Gianni, *Nat. Rev. Clin. Oncol.* **2016**, *13*, 674.

[9] J. A. Zerillo, B. A. Goldenberg, R. R. Kotecha, A. K. Tewari, J. O. Jacobson, M. K. Krzyzanowska, *JAMA Oncol.* **2018**, *4*, 105.

[10] H. Goldvaser, D. Ribnikar, H. Majeed, A. Ocana, E. Amir, *J. Clin. Oncol.* **2018**, *36*, e12501.

[11] K. Li, C. Lin, M. Li, K. Xu, Y. He, Y. Mao, L. Lu, W. Geng, X. Li, Z. Luo, K. Cai, *ACS Nano* **2022**, *16*, 2381.

[12] N. Nayeem, M. Contel, *Chem.- Eur. J.* **2021**, *27*, 8891.

[13] W. Ma, S. Zhang, Z. Tian, Z. Xu, Y. Zhang, X. Xia, X. Chen, Z. Liu, *Eur. J. Med. Chem.* **2019**, *181*, 111599.

[14] Z. Tian, Y. Yang, L. Guo, G. Zhong, J. Li, Z. Liu, *Inorg. Chem. Front.* **2018**, *5*, 3106.

[15] M. H. Chen, F. X. Wang, J. J. Cao, C. P. Tan, L. N. Ji, Z. W. Mao, *ACS Appl. Mater. Interfaces* **2017**, *9*, 133044..

[16] J. S. Nam, M. G. Kang, J. Kang, S. Y. Park, S. J. C. Lee, H. T. Kim, J. K. Seo, O. H. Kwon, M. H. Lim, H. W. Rhee, T. H. Kwon, *J. Am. Chem. Soc.* **2016**, *138*, 109687.

[17] L. He, C. Tan, R. Ye, Y. Zhao, Y. Liu, Q. Zhao, L. Ji, Z. Mao, *Angew. Chem., Int. Ed.* **2014**, *53*, 121371.

[18] J. M. Hearn, G. M. Hughes, I. Romero-Canelón, A. F. Munro, B. Rubio-Ruiz, Z. Liu, N. O. Carragher, P. J. Sadler, *Metallomics* **2018**, *10*, 93.

[19] H. Yuan, Z. Han, Y. Chen, F. Qi, H. Fang, Z. Guo, S. Zhang, W. He, *Angew. Chem., Int. Ed.* **2021**, *60*, 8174.

[20] A. Mondal, S. Shanavas, U. Sen, U. Das, N. Roy, B. Bose, P. Paira, *RSC Adv.* **2022**, *12*, 119536.

[21] a) V. Novohradsky, A. Marco, L. Markova, N. Cutillas, J. Ruiz, V. Brabec, *J. Med. Chem.* **2023**, *66*, 9766; b) L. D. Lavis, *ACS Chem. Biol.* **2008**, *3*, 203; c) K. McClellan, C. M. O Perry, *Drugs* **2001**, *61*, 263; d) P. A. Todd, R. C. E Heel, *Drugs* **1986**, *31*, 198.

[22] J. J. Cao, C. P. Tan, M. H. Chen, N. Wu, D. Y. Yao, X. G. Liu, L. N. Ji, Z. W. Mao, *Chem. Sci.* **2017**, *8*, 631.

[23] S. Kuang, F. Wei, J. Karges, L. Ke, K. Xiong, X. Liao, G. Gasser, L. Ji, H. Chao, *J. Am. Chem. Soc.* **2022**, *144*, 4091.

[24] F. X. Wang, M. H. Chen, X. Y. Hu, R. R. Ye, C. P. Tan, L. N. Ji, Z. W. Mao, *Sci Rep.* **2016**, *6*, 38954.

[25] G. Marverti, G. Gozzi, A. Lauriola, G. Ponterini, S. Belluti, C. Imbriano, M. P. Costi, D. D'Arca, *Int. J. Mol. Sci.* **2019**, *20*, 6122.

[26] R. D. Costa, E. Ortí, H. J. Bolink, F. Monti, G. Accorsi, N. Armaroli, *Angew. Chem., Int. Ed.* **2012**, *51*, 8178.

[27] S. Ladouceur, D. Fortin, E. Zysman-Colman, *Inorg. Chem.* **2011**, *50*, 115146.

[28] J. S. Nam, M. G. Kang, J. Kang, S. Y. Park, S. J. C. Lee, H. T. Kim, J. K. Seo, O. H. Kwon, M. H. Lim, H. W. Rhee, T. H. Kwon, *J. Am. Chem. Soc.* **2016**, *138*, 109687.

[29] N. Singh, A. Gupta, P. Prasad, R. K. Sah, A. Singh, S. Kumar, S. Singh, S. Gupta, P. K. Sasmal, *J. Med. Chem.* **2021**, *64*, 178133.

[30] X. Q. Zhou, P. Wang, V. Ramu, L. Zhang, S. Jiang, X. Li, S. Abyar, P. Papadopoulou, Y. Shao, L. Bretin, M. A. Siegler, F. Buda, A. Kros, J. Fan, X. Peng, W. Sun, S. I. Bonnet, *Nat. Chem.* **2023**, *15*, 980.

[31] a) Q. Du, L. Zhao, L. Guo, X. Ge, S. Zhang, Z. Xu, Z. Liu, *Appl. Organomet. Chem.* **2019**, *33*, e4746; b) X. Q. Zhou, M. Xiao, V. Ramu, J. Hilgendorf, X. Li, P. Papadopoulou, M. A. Siegler, A. Kros, W. Sun, S. Bonnet, *J. Am. Chem. Soc.* **2020**, *142*, 103839; c) Q. Zhong, J. Zeng, X. Jia, *Int. J. Nanomed.* **2024**, *19*, 5931; d) A. Sosnik, *Prog. Mater. Sci.* **2016**, *82*, 39; e) K. Yue, J. Tang, H. Tan, L. Xiao-xing, X. Zhang, *J. Heat Transf.* **2017**, *140*, 012003; f) W. R. Zhuang, Y. Wang, P. F. Cui, L. Xing, J. Lee, D. Kim, H. L. Jiang, Y. K. Oh, *J. Controll. Rel.* **2019**, *294*, 311.

[32] X. Zhao, J. Zhang, W. Zhang, Z. Guo, W. Wei, X. Wang, J. Zhao, *Chem. Sci.* **2023**, *14*, 1114.

[33] Y. Xie, W. Hou, X. Song, Y. Yu, J. Huang, X. Sun, R. Kang, D. F Tang, *Cell Death Differ.* **2016**, *23*, 369.

[34] M. Shee, D. Zhang, M. Banerjee, S. Roy, B. Pal, A. Anoop, Y. Yuan, N. D. P. Singh, *Chem. Sci.* **2023**, *14*, 9872.

[35] E. H. W. Pap, G. P. C. Drummen, J. A. Post, P. J. Rijken, K. W. A. Wirtz, *Meth. Enzymol.* **2000**, *54*, 603.

[36] S. Sen, S. Hufnagel, E. Y. Maier, I. Aguilar, J. Selvakumar, J. E. DeVore, V. M. Lynch, K. Arumugam, Z. Cui, J. L. Sessler, J. F. Arambula, *J. Am. Chem. Soc.* **2020**, *142*, 205361.

[37] A. A. Rowland, G. K. Voeltz, *Nat. Rev. Mol. Cell Biol.* **2012**, *13*, 607.

[38] G. Csordás, C. Renken, P. Várnai, L. Walter, D. Weaver, K. F. Buttle, T. Balla, C. A. Mannella, G. Hajnóczky, *J. Cell Biol.* **2006**, *174*, 915.

[39] A. P. King, J. J. Wilson, *Chem. Soc. Rev.* **2020**, *49*, 8113.

[40] J. R. Cubillos-Ruiz, S. E. Bettigole, L. H. Glimcher, *Cell* **2017**, *168*, 692.

[41] C. J. Adams, M. C. Kopp, N. Larburu, P. R. Nowak, M. M. U. Ali, *Front. Mol. Biosci.* **2019**, *6*, 1.

[42] B. Rah, D. Nayak, R. Rasool, S. Chakraborty, A. Katoch, H. Amin, A. Goswami, *Curr. Mol. Med.* **2016**, *16*, 690.

[43] a) I. Kuznetcova, F. Bacher, S. M. Alfadul, M. Jing, W. H. Ang, M. V. Babak, P. Rapta, V. B. Arion, *Inorg. Chem.* **2022**, *61*, 101671; b) C. M. Oslowski, F. Urano, *Meth. Enzymol.* **2011**, *490*, 71; c) W. Yan, C. L. Frank, M. J. Korth, B. L. Sopher, I. Novoa, D. Ron, M. G. Katze, *Proc. Natl. Acad. Sci. USA* **2002**, *99*, 159205.

[44] A. Bertolotti, Y. Zhang, L. M. Hendershot, H. P. Harding, D. Ron, *Nat. Cell Biol.* **2000**, *2*, 326.

[45] L. Wang, R. Guan, L. Xie, X. Liao, K. Xiong, T. W. Rees, Y. Chen, L. Ji, H. Chao, *Angew. Chem., Int. Ed.* **2021**, *60*, 4657.

[46] a) J. J. Cao, Y. Zheng, X. W. Wu, C. P. Tan, M. H. Chen, N. Wu, L. N. Ji, Z. W. Mao, *J. Med. Chem.* **2019**, *62*, 3311; b) R. Skouta, S. J. Dixon, J. Wang, D. E. Dunn, M. Orman, K. Shimada, P. A. Rosenberg, D. C. Lo, J. M. Weinberg, A. Linkermann, B. R. Stockwell, *J. Am. Chem. Soc.* **2014**, *136*, 4551; c) Krusenstiern, R. N. Robson, N. Qian, B. Qiu, F. Hu, E. Reznik, N. Smith, F. Zandkarimi, V. M. Estes, M. Dupont, T. Hirschhorn, M. S. Shchepinov, W. Min, K. A. Woerpel, B. R. Stockwell, *Nat. Chem. Biol.* **2023**, *19*, 719; d) M. M. Gaschler, F. Hu, H. Feng, A. Linkermann, W. Min, B. R. Stockwell, *ACS Chem. Biol.* **2018**, *13*, 1013.

[47] a) T. R. Panda, Manikandan M, S. P. Vaidya, S. Chhatar, S. Sinha, M. Mehrotra, S. Chakraborty, S. Gadre, P. Duari, P. Ray, M. Patra, *Angew. Chem., Int. Ed.* **2023**, *62*, 202306179; b) J. Cao, Y. Zheng, X. Wu, C. P. Tan, M. H. Chen, N. Wu, L. N. Ji, Z. W. Mao, **2019**, *62*, 3311.

[48] R. Naik, J. Seetharamappa, *J. Fluoresc.* **2023**, *33*, 13.

[49] S. P. Vaidya, Manikandan M, S. Chhatar, S. Dey, C. Patra, M. A. Patra, *Inorg. Chem. Front.* **2023**, *10*, 6711.

[50] T. C. Chou, *Pharmacol. Rev.* **2006**, *58*, 621.

[51] A. S. Nunes, A. S. Barros, E. C. Costa, A. F. Moreira, I. J. Correia, *Biotechnol. Bioeng.* **2019**, *116*, 206.

[52] a) J. Friedrich, C. Seidel, R. Ebner, L. A. Kunz-Schughart, *Nat. Protoc.* **2009**, *4*, 309; b) Y. Lu, S. S. Wang, M. Y. Li, R. Liu, M. F. Zhu, L. M. Yang, F. Y. Wang, K. B. Huang, H. Liang, *Acta Pharm. Sin. B* **2024**, https://doi.org/10.1016/j.apsb.2024.06.017; c) Y. Hao, Z. Han, Y. Chen, F.

Qi, H. Fang, Z. Guo, S. Zhang, W. He, *Angew. Chem., Int. Ed.*, *60*, 8174; d) M. Lv, Y. Zheng, J. Wu, Z. Shen, B. Guo, G. Hu, Y. Huang, J. Zhao, Y. Qian, Z. Su, C. Wu, X. Xue, H. Liu, Z. Mao, *Angew. Chem., Int. Ed.* **2021**, *2023*, 62; e) H. Hu, F. Zhang, Z. Sheng, S. Tian, G. Li, S. Tang, Y. Niu, J. Yang, Y. Liu, *Eur. J. Med. Chem.* **2024**, *268*, 11629595; f) X. Zhao, J. Zhang, W. Zhang, Z. Guo, W. Wei, X. Wang, J. Zhao, *Chem. Sci.* **2023**, *14*, 1114; g) W. Wang, Y. Ling, Y. Zhong, Z. Li, C. Tan, Z. Mao, *Angew. Chem., Int. Ed.* **2022**, *61*, 202115247.

[53] G. J. Lin, G. B. Jiang, Y. Y. Xie, H. L. Huang, Z. H. Liang, Y. J. Liu, *J. Biol. Inorg. Chem.* **2013**, *18*, 873.

[54] P. Hohenberg, W. Kohn, *Phys. Rev.* **1964**, *136*, B864.

[55] W. Kohn, L. J. Sham, *Phys. Rev.* **1965**, *140*, A1133.

[56] W. N L Kohn, *Rev. Mod. Phys.* **1999**, *71*, 1253.

[57] M. J. Frisch, G. W. Trucks, H. B. Schlegel, G. E. Scuseria, M. A. Robb, J. R. Cheeseman, G. Scalmani, V. Barone, G. A. Petersson, H. Nakatsuji, X. Li, M. Caricato, A. V. Marenich, J. Bloino, B. G. Janesko, R. Gomperts, B. Mennucci, H. P. Hratchian, J. V. Ortiz, A. F. Izmaylov, J. L. Sonnenberg, D. Williams-Young, F. Ding, F. Lipparini, F. Egidi, J. Goings, B. Peng, A. Petrone, T. Henderson, D. Ranasinghe, et al., Fox, D. J. G. Inc, W. C. Gausian *16*, **2016**.

[58] P. J. Hay, W. R. Wadt, *J. Chem. Phys.* **1985**, *82*, 299.

[59] a) W. R. Wadt, P. J. Hay, *J. Chem. Phys.* **1985**, *82*, 284; b) B. Zhao, Z. Ma, S. Ding, Y. Cao, J. Du, L. Zeng, Y. Hu, J. Zhou, X. Zhang, X. Bian, G. Tian, *Adv. Funct. Mater.* **2023**, *33*, 2306328.

[60] a) P. J. Hay, W. R. Wadt, *J. Chem. Phys.* **1985**, *82*, 270; b) B. Feng, Z. Niu, B. Hou, L. Zhou, Y. Li, *Adv. Funct. Mater.* **2019**, *30*, 1906605.

[61] H. R. Drew, R. M. Wing, T. Takano, C. Broka, S. Tanaka, K. Itakura, R. E. Dickerson, *Proc. Natl. Acad. Sci. USA* **1981**, *78*, 2179.